Influence of Precipitation and Land Use on Pore Geometry in Soils with Vertic Properties

By

Matthew G. Sena

B.S., Environmental, Soil, and Water Science – University of Arkansas, Fayetteville

Submitted to the graduate degree program in Department of Geography and Atmospheric Science and the Graduate Faculty of the University of Kansas in partial fulfillment of the requirements for the degree of Master of Science.

Chair: Nathaniel A. Brunsell

Sharon A. Billings

Bing Pu

Pamela L. Sullivan

Daniel R. Hirmas

Date Defended: 17 July 2020

The thesis committee for Matthew G. Sena certifies that this is the approved version of the following thesis:

Influence of Precipitation and Land Use on Pore Geometry in Soils with Vertic Properties

_____

Co-Chair: Co-Chair Name

_____

Co-Chair: Co-Chair Name

Date Approved: 17 July 2020

Abstract

Soil aggregates, a fundamental unit of soil structure, are formed when minerals and organic matter bind together. Physiochemical drivers, such as soil texture and organic carbon (OC), help govern soil aggregate resiliency to changes in climate, vegetative land cover, and anthropogenic pressures. These drivers in turn shape the spacing between aggregates upon which water is stored and moved through the Earth's critical zone (CZ). Recent evidence suggests that soil structure may be changing on decadal timeframes as a result of differences in moisture conditions leading to potentially significant changes in soil hydraulic properties (e.g., saturated hydraulic conductivity, Ksat). Soil macropore geometry, determined through multistripe laser triangulation (MLT), and shrink-swell behavior, assessed through measures of the coefficient of linear extensibility (COLE), can be related to Ksat to predict how future climatic and land use conditions will influence soil water stores and fluxes. Additionally, findings from this study can be related to more qualitative, field descriptions such as horizon thickness and soil structural classification.

In this research we used precipitation (580-1012 mm; semiarid-to-mesic at Hays, Konza, and Welda) and land use (Native, Post-Agriculture, and Agriculture) gradients across Kansas to quantitatively explore these relationships. To characterize the influence of climate/land cover-induced changes on pore geometry and hydraulic properties in shrink-swell soils and relate these measures to soil moisture, we collected soil monoliths from the face of ~2 m deep soil pits located under three land use types with three differing precipitation regimes, and installed soil moisture sensors at three depths (10, 40, and 120 cm). Key results from this work showed that: 1) pore aspect ratio and the tortuosity coefficient generally increased with depth, especially at Native sites, 2) pore density (Dssg) at depth was greatest at drier sites (Hays) compared to wetter sites (Konza and Welda), and 3) the effective pore area (Aeff) increased with decreasing mean annual precipitation (MAP), which was concurrent with lower COLE, clay, and OC contents, but little change in pore width (min Feret diameter when measured at a dry state). Land use, particularly at row-crop Agricultural sites, alters the nature of these relationships. For example, mean aspect ratio and tortuosity coefficients were higher at Agricultural than Native land uses for both the near surface and subsurface horizons. We can infer that the observed decline in Aeff with increased MAP at our sites results in a decline in Ksat, as previously reported work showed a positive relationship between Ksat and Aeff. Soils scanned through MLT can provide more detailed, quantitative-based metrics that can improve estimates of hydrologic fluxes.

Acknowledgements

I would like to thank my family, particularly Mom, Dad, and Michael, as well as my friends, whether in Memphis, Fayetteville, Lawrence, or elsewhere; words cannot describe my appreciation for your love and support over the years. Because of you I continue to grow as a person and discover things that I am passionate about every day. My academic committee, Pamela Sullivan, Daniel Hirmas, Sharon Billings, Nathaniel Brunsell, and Bing Pu, have been there every step of the way and have taught me countless invaluable lessons in terms of research across the fields of soil science, hydrology, biology, and atmospheric science. This work would not have been possible without your sustained encouragement and guidance. I am also grateful for funding from Kansas EPSCoR by the NSF OIA-1656006 and matching support from the State of Kansas through the Kansas Board of Regents and NSF EAR-1841614. Any opinions, findings, and conclusions or recommendations expressed in this material are those of the author(s) and do not necessarily reflect the views of the National Science Foundation.

Table of Contents

1 Introduction

Recent evidence suggests that soil structure may be changing on decadal timeframes as a result of changes in moisture availability (Hirmas et al. 2018); these changes have the potential to influence the hydrologic cycle, and land surface-atmosphere energy fluxes, and, thus, climate (Franzluebbers, 2002; Nissen & Wander, 2003; Seneviratne et al., 2010). Specifically, changes in environmental drivers (e.g., moisture conditions) can influence wet-dry cycles, durations of "sealed" pores, and carbonate accumulation that can alter the geometry of pores, their connectedness, and tortuosity coefficients (Gunal & Ransom, 2006; Stewart et al., 2015; Figure 1). These interactive feedbacks shape the hydraulic properties and their ability to fluctuate over time. It is well established that the structure of soil is directly influenced by climate over long periods of time (Jenny, 1941; Mohammed et al., 2020), but new evidence suggests that changes in wet-dry and freeze-thaw processes affect soil aggregation and soil structure over short time periods too (Figure 1; Robinson et al., 2016; Robinson et al., 2019). Biotic factors such as organic carbon cycling, root growth, and vegetative cover are also influenced by changes in moisture availability (Seneviratne et al., 2010) and can feedback to govern soil water content, all of which play a role in aggregate stability and size (Mohammed et al., 2020). While climate-induced soil structural changes have been inferred across an array of soil types (e.g., Hirmas et al. 2018), their influence on the hydraulic properties of soils with a high shrink-swell capacity has not been investigated directly, nor have their temporal dynamics on hydraulic properties been assessed across a range in moisture conditions.

Soil aggregation, or the process of aggregate formation that determines soil structure, is a crucial process in the Earth's critical zone (CZ) and is influenced by environmental factors such as climate, vegetative land cover, and anthropogenic disturbance. Soil aggregates, and their packing arrangement, which can range in scales from submillimeter clusters of particles to coarse peds, represent fundamental units of structure. One important process that drives aggregation is through the interaction of clay content, mineralogy, and soil organic matter (SOM), where aggregates are often negatively charged and attract SOM through adsorption (McBride, 1989). The presence of SOM on the outer coating of soil peds improves their stability by increasing their hydrophobicity, thus making them more water-stable and less water-dispersible (Oades, 1989). Microorganisms also contribute to the formation of soil aggregates. For example, by releasing extracellular

polymeric substances (EPS), microbes can promote macroaggregates (> 250 μm in diameter) from the cohesion of microaggregates (< 250 μm in diameter) (Banwart et al., 2011).

Vegetation and microorganisms form complex relationships in the soil that play a significant role in soil-carbon dynamics, and, thus, aggregate stability. Plants provide both exudates through roots that promote microbial activity (Kuzyakov 2010; Blagodatskaya & Kuzyakov, 2008) as well as soil organic carbon (SOC) in the form of cellulose-and-lignin-rich plant litter (Thevenot et al., 2010), which may prime microorganism-driven decomposition that increases the rate of SOC consumption (Fontaine et al., 2004; Heitkamp et al., 2012; Weismeier et al., 2016). As pores approach saturation, available oxygen becomes depleted and microbes use less energy-efficient pathways in respiration. Reduction in respiration efficiency may lead to the consumption of carbon dioxide and the release of methane under prolonged saturated conditions (Bosse & Frenzel, 1997). Thus, the interaction between aggregation processes and their impact on pore geometry can create feedbacks that control soil moisture conditions and soil biotic processes, which in turn shapes the geometry of pores.

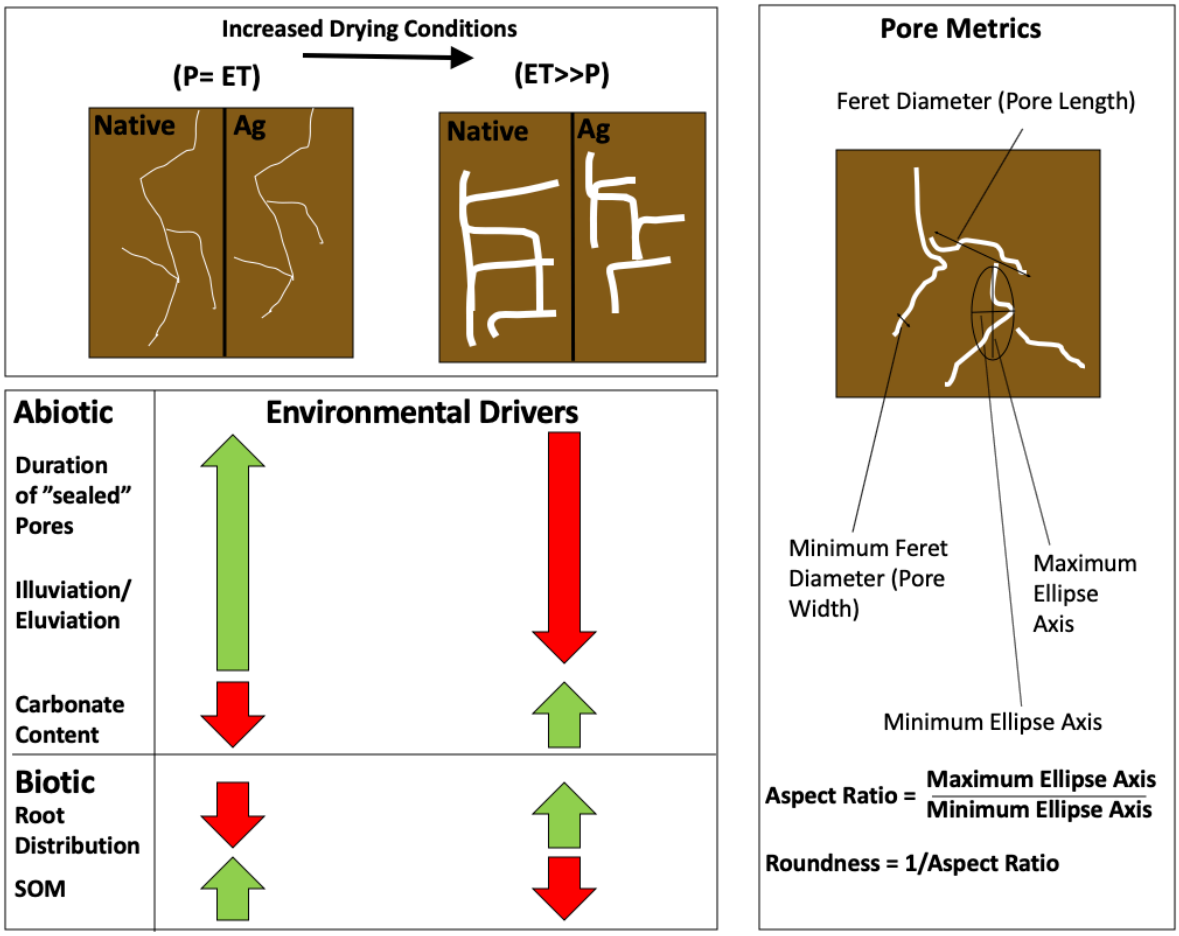

Figure 1 - Conceptual diagram showing the effect of biotic and abiotic processes that drive shrinking and swelling of macropores within the soil.

When the soil matrix swells the pore spaces seal, which can influence aggregate stability by altering soil processes such as oxygen availability, water infiltration, storage (Franzluebbers, 2002), erosion, crusting, nutrient cycling, and root penetration (Bronick & Lal, 2005). As soil systems respond to changing climatic pressures, as well as differences in lithology (e.g. parent source material), they can alter the density and distribution of macropores — continuous openings or voids in the soil > 1 mm in diameter that affect water flow (Luxmoore et al., 1990). These voids connect to form 3-dimensional networks that can be continuous for meters in both vertical and lateral directions (Beven & Germann, 1982). Altogether macropores typically make up ~1% of the soil matrix, they control ~70% of the water flux through the soils (Watson and Luxmoore, 1986) making their dynamic response to climate and other drivers key for projecting hydrologic fluxes

(Beven & Germann, 1982; Franzluebbers, 2002; Nissen & Wander, 2003). We often relate macropores to the effective porosity (EP) of soils, which is the portion of rock or sediment media that has the ability to contribute to fluid flow (Fetter, 1993; Domenico & Schwartz, 1990) and can be estimated as the difference between total porosity and field capacity — the remaining water content following drainage by gravitational forces (Rawls et al., 1998). The Kozeny-Carman equation allows us to use EP in order to predict saturated hydraulic conductivity (Ksat) — the ability of water to be conducted through saturated porous media (Smith, 2002; McCuen, 2003). Yet, these values do not inherently account for the physical architecture of these pores. Pedotransfer functions (PTFs), particularly ROSETTA (Schaap et al., 2001) are also a means to derive soil hydraulic properties from available soil properties (e.g., sand, silt, clay, and bulk density) (Van Looy et al, 2017) but, generally speaking, they do not include metrics of soil structure and often only represent the hydraulic properties of the soil matrix. One recent exception to this is the derivation of PTF in the Carbon, Aggregation, and Structure Turnover (CAST) model which incorporates soil structural information to predict hydraulic properties over a variety of land uses and management practices (Li et al., 2017). New numerical methods are also starting to emerge to account for shrink-swell dynamics on soil hydraulic properties (e.g., Stewart et al., 2016). Overall these advances help to guide how we represent water flow and water budgets from local to even global scale models (Van Looy, 2017). As a result, advances in our understanding of relationships between climate, soil structure, the arrangement of pores, and, thus, soil hydraulic properties can be scaled to understand its feedback to the hydrologic cycle and climate.

The key now is deriving more quantitative relationships between soil hydraulic properties, structure, pore space, chemistry and the aggregate stability "life-cycle"- the process in which aggregates form and become more water stable through the enmeshment of organic carbon (Banwart et al., 2011). For decades methods of quantifying soil structure relied on more qualitative techniques such as visual inspection, dye studies, and smoke injections that provide only proxies for soil structure (Allaire et al., 2009). Likewise, traditional spectroscopy-based techniques for quantifying chemical distributions often require destructive homogenization that reduces accuracy when analyzing a natural soil profile (Steffens et al., 2014). Given the advent of high spatial resolution tools (Banwart et al., 2011) it is now possible to use more accurate quantitative approaches. For example, soil structure can be quantified using high-resolution laser scanning (multistripe laser triangulation (MLT)), which has the ability to capture pores larger than 125 μm

in diameter. This technique effectively digitizes soil macropores > 3.14 mm^2 and thus allowing for the quantification of soil pore geometry (Eck et al., 2013; Hirmas et al., 2013). The scanner specifically measures gaps in the soil that can be used to represent the size, shape, orientation, and abundance of macropores (Eck et al., 2013; Eck et al., 2016).

Given the importance of macropores on soil hydrology, advancing the ability to make hydrologic predictions requires addressing a fundamental knowledge gap: *how do we relate climate, soil physical/ chemical properties (structure, texture, and chemical distributions) and soil hydraulic properties, especially in soils that contain a high shrink-swell capacity (Eck et al., 2016)?* Hydrologic and pedogenic modeling must be expanded to include precipitation regimes and land use types. This research aims to address this knowledge gap in soil structure by using the natural laboratory of Kansas to examine soil structure over a precipitation gradient (mean annual precipitation, MAP, from 580 to 1012 mm), across land use types (Agriculture, Post-Agriculture, and Native Prairie), and where soil contains a high shrinks swell capacity (Midwestern Mollisol soils with montmorillonite clay). Specifically, this research aims to test two hypotheses:

(H1) Macropore geometry in soils with vertic properties will be indirectly influenced by the frequency/intensity and total annual precipitation as they govern aggregate-sensitive soil properties such as soil organic carbon and soil texture. Soils that developed under lower MAP with less frequent wet-dry cycles will have lower organic carbon and clay contents which will result in macropore expression that has greater Aeff and, thus, saturated hydraulic conductivity than wetter sites with more frequent wet-dry cycles.

(H2) Intensive land use confounds the influence of precipitation on macropore geometry, where the link between OC and texture with pore metrics such as tortuosity coefficients, Aeff, and aspect ratio will show more variable, less linear trends with environmental drivers across the precipitation gradient.

2 Study Area

To investigate the impact of soil forming factors (Jenny 1941) on controlling pore geometry, three sites were selected across the natural rainfall gradient in Kansas: Hays, Konza, and Welda (driest to wettest) (Figure 2 and Table 1). We focused on the interaction of climate, lithology, shrink-swell capacity, organic carbon content, and root abundance on pore metrics such as length, angle, and roundness. The Kansas State University Agricultural Research Center (38.8° N, 99.3164° W), located in the West-Central Kansas Smoky Hills region, represented the driest site (Hays), while Konza Prairie Biological Research Station (KPBS; 39.1069° N, 96.6091° W) located ~10 km south

of Manhattan, KS represented the middle of the precipitation gradient (Konza). Finally, two sites near Welda (Native and Post-Agricultural sites) (38.1811° N, 95.4742° W) and Ottawa (Agricultural site) (38.5387° N, 95.2472° W), separated by ~ 40 km in Eastern Kansas near Ottawa, KS represented the wet end of the transect. Three land uses were examined at each site: 1) Native prairie - prairies never used for row-crop agriculture but subject to mowing and burning practices, 2) Post-Agricultural (Post-Ag) sites - prairies that have a legacy of row-crop agriculture, and 3) Agricultural sites, which were under current row-crop practices and irrigation was not applied.

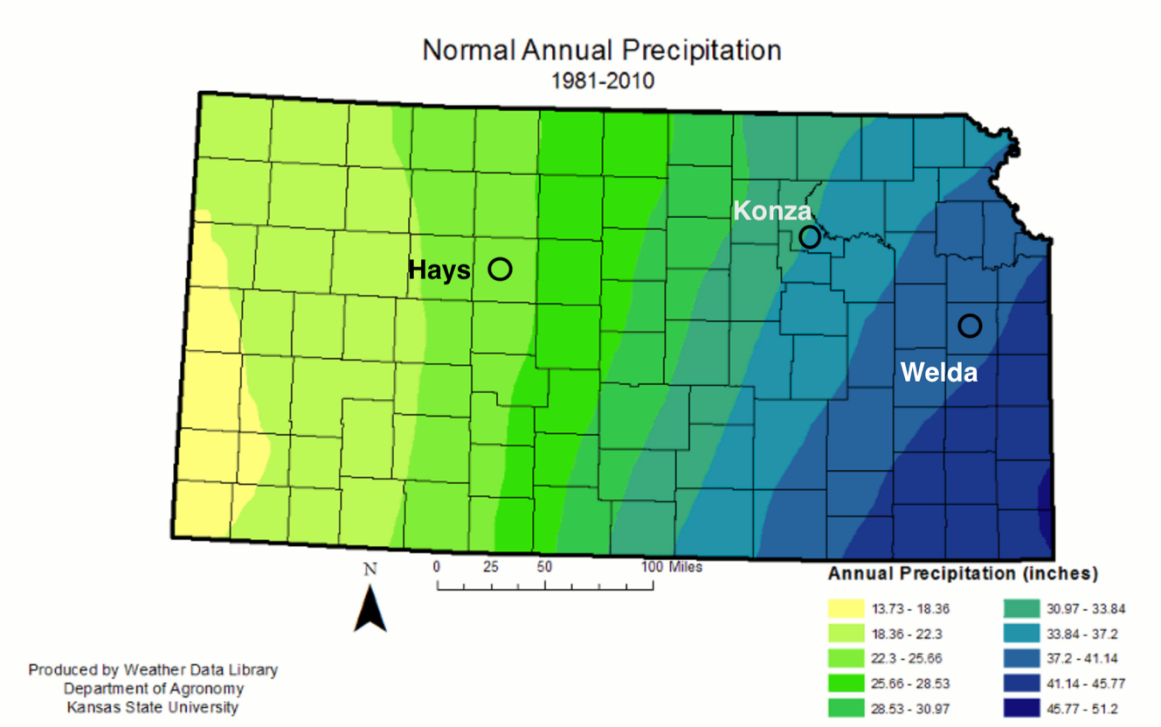

Figure 2 - Location of three field sites (Welda, Konza, Hays) across the strong rainfall gradient that persists in Kansas, USA.

Table 1 - Comparison of region, elevation, climate, and root averages across pits sampled for each site. Root data are from Souza et al. (in prep).

	Hays	Konza	Welda
Geomorphic Region	Smoky Hills	Flint Hills	Osage Cuestas
Elevation (m)	616	330	335
Mean Annual Prepitation (mm)	580	835	1,012
Mean Annual High Temperature (°C)	19.5	19.5	18.7
Mean Annual Low Temperature (°C)	4.9	5.9	6.6
Mean Annual Days below Freezing (0 °C)	126	114	98
Mean Total Roots/ cm	12.4 +/- 7.2	27.1 +/- 8.6	23.4 +/- 6.5
Mean Fine Roots/ cm	9.7 +/- 5.0	22.4 +/- 7.9	17.1 +/- 6.3
Mean Coarse Roots/ cm	2.6 +/- 3.1	4.6 +/- 8.1	6.3 +/- 5.2
** Standard deviations across sites, not by horizon.			

2.1 Climatic differences

Mean annual precipitation increases from 580 mm to 835 mm to 1012 mm (https://www.usclimatedata.com) at Hays, Konza, and Welda, respectively. Although the mean annual temperature (MAT) across all sites are similar (12.1 - 12.7 ºC), the variation throughout the year declines eastward, with an annual range of 14.6 ºC at Hays, 13.6 ºC at Konza, and 12.1 ºC at Welda. Mean annual days below freezing also decrease in this direction, providing less opportunity for freeze-thaw fluctuations in the soil at Welda compared to Hays (https://weatherspark.com/; Table 1). Analysis of long term (1988 - 2017) precipitation data indicates that frequency and duration patterns of precipitation differ between sites (Loecke et al., in prep). Here, two metrics were used: the maximum consecutive dry days (CDD) where < 1 mm of precipitation fell, and maximum 5-day precipitation total (R5D). The median CDD declined by ~ 25% between Hays (40 ± 14.3 days) and Konza and Welda (29.5 ± 8.7 days and 26.5 ± 8.8 days, respectively). The median R5D was lowest at Hays with values 81.5 ± 28.9 mm, increased at both Konza and Welda 105.0 ± 26.8 mm and 111.6 ± 63.4 mm, respectively. These data indicate that while the MAP differs between the three sites, the frequency, intensity, and duration patterns of the two wetter sites (Konza and Welda) are similar; where both the frequency, intensity, and duration of precipitation events were lower at Hays.

2.2 Lithologic Setting

The parent material sources for soil development change drastically when moving east to west in Kansas, which has implications for how the properties of developed soil respond to precipitation events. The lithology of Ellis County and Smoky Hills Region, where Hays is located, consists of mostly Quaternary to Cretaceous age rock (KGS, 1926), including deposited loess at the surface,

predominantly in the upland landscape positions of the Saline and Smoky Hill River valleys (Welch & Hale, 1987). Konza is located within the Flint Hills, which are upland escarpments within a temperate midcontinental climate (Bark, 1987). The Flint Hills express a unique terraced, or "benched" shape facing the east-west directions along with a limestone cap containing a significant amount of flint, which makes it more resistant to weathering (Schoewe, 1949). Welda is located within the Osage Cuestas, similar formations to the Flint Hills, which are a series of escarpments made of alternating layers of Pennsylvanian-age limestone and shale with a short, sharp slope on one side, and a long gentle slope on the other. Over time, differential erosion occurs as a result of the limestone and shale weathering unevenly; thus, producing the cuesta (Schoewe, 1949).

2.3 Soils

In order to compare differences in soil properties, particularly shrink-swell in clays, soil descriptions performed by the NRCS were compared across precipitation and land-use gradients. All soils across sites were described as Mollisols and most with vertic or smectitic mineralogies, except at the Konza Native site. Soils at Hays was described as fine, smectitic, mesic Typic Argiustolls. With the exception of the Native site, Mollisols at Konza showed vertic descriptions, as opposed to smectitic descriptions at Hays. Soils under Native vegetation at the Native site were classified as fine, mixed, superactive, mesic Pachic Argiustolls, while those under Post-Agriculture were classified as fine, mixed, superactive, mesic Pachic Vertic Argiudolls. Soils were classified as fine-silty, mixed, superactive, mesic Pachic Vertic Argiudolls within the Agricultural land use at Konza. Soils at Welda were classified with both smectitic families and vertic subgroups, with the Native soil classified as a loamy-skeletal, smectitic, thermic Aquertic Argiudolls at the Native prairie, fine, smectitic, thermic Oxyaquic Vertic Argiudolls at the Post-Agricultural land use, fine-silty, mixed, superactive, mesic Pachic Vertic Argiudolls under the Agriculture land use.

2.4 Roots

Given that roots influence soil structure through root exudation and respiration of organic carbon, and can generate or clog macropores, the pore data generated from MLT scans will be compared to measures of root abundance. Specifically, Souza et al. (in prep) measured total, fine (< 0.1 cm diameter), and coarse (> 0.1 cm diameter) root abundances across all nine sites. They observed that overall root abundance for Native and Post-Agriculture sites decreased for total, fine, and coarse roots as precipitation decreased (e.g., Hays had the lowest total, fine, and coarse root

abundance). For the Agricultural sites, total, fine, and course root abundance was greatest at Konza and lowest at Welda. This information is important to place in the context of overall vegetation changes across the Kansas precipitation gradient, as roots contribute to organic carbon in the soil, where Konza and Welda are predominantly tall-grass prairie ecosystems (Climatology, 1987; Norris et al., 2001) and Hays is a mix of short-and tall-grass prairies (Albertson, 1937).

3 Methods

To test that precipitation and land-use gradients systematically control soil properties and, thus, the expression of macropore geometry soil monoliths and samples were collected across the nine sites. Soil moisture sensors were also installed at each location in order to relate macropore metrics to soil moisture conditions and understand the degree to which shrink-swell processes play a role in pore properties. We then related soil physical and chemical properties to climatic conditions using the soil moisture data collected in this study as well as 2018 – 2020 Mesonet precipitation data. In addition, root data collected from each of the sites (Souza et al. in prep) were used to compare differences in drivers across land cover types.

3.1 Field work

3.1.1 Monolith, sample collection

Monoliths were collected from nine, 2-meter deep soil pits excavated by the NRCS, to quantify the soil pore geometry across precipitation and land-use gradients in Kansas. Monolith trays were two sizes: either 40 or 20 cm tall by 30 cm wide and 4 cm deep; these allowed for flexibility in capturing the greatest proportion of a single horizon within tray (Appendix A). Depending on the site, 5 - 7 trays were used to collect samples from ground surface until roughly ~1.9 m deep. To excavate the monoliths, field knives and rock hammers were used to carve out the perimeter around each tray at approximately a 4 cm depth. Trays were then pressed onto the soil reliefs and field knives were then wedged around each soil tray to separate it from the soil face. Care was taken to ensure 3-5 cm of overlap between each tray such that as little information was lost with depth. After the trays were excavated, they were leveled using trowels and field knives, labeled, and wrapped before transporting to the lab for analysis. In the time between field excavation and lab analysis, the soils will be placed in a cooled (0 - 5 °C) storage room. At the time of scanning, one soil sample was collected for each horizon excavated; 1 gram of soil from each horizon was placed

into three tins and dried at 105 °C for 24-48 hours in order to determine gravimetric moisture content at the time of scanning.

3.1.2 Soil Sensor Monitoring Arrays

Soil moisture and temperature (METER Group ECH$_2$O 5TM) were measured at three depths (10, 40, and 120 cm) to better understand the variations in subsurface hydrologic conditions across the precipitation and land-use gradients (Appendix B). Sensors were connected to a Campbell Scientific CR1000X datalogger, powered by a 12V power supply and solar panel, and data were obtained at a 30 min rate of collection. Each datalogger was programmed through CRBasic and the data was accessed through LoggerNet (Campbell Scientific Inc., Logan UT) via direct USB connection.

3.2 Lab Analyses

3.2.1 NRCS Soil Analyses

Along with describing the pits in detail, soil samples were collected by horizon and analyzed by the NRCS for numerous soil physical/ chemical properties including particle size, EOC, pH, and cation exchange capacity (CEC) (Soil Survey Staff, 2014). Particle-size distribution was determined using the pipette method, and bulk density at oven dry and 0.33 bar was obtained using the clod method. Soil hydraulic information such as field capacity ($\theta_{0.33}$), that is, the point at which water stops flowing under the influence of gravity and wilting point (θ_{15}), as well as air-dried / oven-dried ratio (ADOD) were also collected. From these data we calculated total porosity (*n*) and effective porosity (*EP*), where *n (%)*:

$$n = 100 - \left(\frac{BD_{od}}{Pd}\right) 100 \qquad \text{Eq. (1)}$$

where BD_{od} is the oven-dry bulk density and P_d is the particle density. Particle density was assumed to be 2.56 g/cm^3. *EP* was calculated by taking the difference between total porosity and field capacity. The COLE method, as performed by the NRCS, compares a volumetric change of a soil clod by measuring a ratio of BD_{od} to bulk density of soil at 33 kPa (BD_{33}) using the following equation (Soil Survey Staff, 2014):

$$\text{COLE} = (BD_{33}/\ BD_{od})^{1/3} - 1 \qquad \text{Eq. (2)}$$

3.2.2 MLT Procedure

To expose the natural soil surface and best represent pore geometries from the MLT scan, soil faces were frozen following Hirmas et al. (2013) and dental tools were used to remove ~ 0.5 cm of soil. Soil trays were then dried for several days in order to enhance the expression of macropores as the soil surfaces shrank (Appendix C). We obtained surface scan gaps (SSGs) —by sub-scanning trays 6.5" below the MLT scanner using the software ScanStudio HD (NextEngine Inc., Santa Monica, CA). Each sub-scan was later aligned and superimposed with other sub-scans with a 2.5 cm overlap to produce one coherent image depicting voids (pores) and solids (soil). Trays were then trimmed to contain a single soil horizon, converted into .xyz files, and processed in ImageJ to generate a series of macropore metrics (Table 2; Eck et al., 2013; Eck et al., 2016). All pores with areas > 3.14 mm^2 (corresponding to the max area of a sand grain) were then analyzed across precipitation and land-use gradients.

Table 2 - Macropore metrics that were analyzed from the collected soil trays (Eck et al., 2013; Eck et al. 2016).

Metric	Variable	Formula	Description
Size			
Area (mm^2)	A		Expressed as $A^{1/2}$ (mm) when comparing as the side length of a square with an equivalent area.
Perimeter (mm)	P		Expressed as P/4 (mm) when comparing to the side length of a square with an equivalent area
Major Ellipse Axis (mm)	E_{MAJ}		Equivalent area, same orientation and centroid as SSGs for which ellipse is drawn
Minor Ellipse Axis (mm)	E_{MIN}		Equivalent area, same orientation and centroid as SSGs for which ellipse is drawn
Feret Diameter (mm)	F		Maximum caliper distance (i.e., longest distance between parallel tangents to the SSG)
Minimum Feret Diameter (mm)	F_{MIN}		Minimum caliper distance
Cross-Sectional Area (mm^2)	A_{XS}		For each horizon or area of interest; Used to calculate SSG density, fraction, relative surface area, and average unit size
Total SSG Area (mm^2)	A_{SSG}	$(N \Sigma i=l) A_i$	
Total SSG Perimeter (mm)	P_{SSG}	$(N \Sigma i=l) P_i$	
Relative SSG Surface Area (mm^-1)	Arel	P_{SSG}/A_{XS}	
Average Unit Size (mm)	U_S	$[(Axs - A_{SSG})*4]/(P_{SSG})$	Units (i.e., soil aggregates and peds) are outlined by SSGs
SSG Fraction	SSG_F	A_{SSG}/A_{XS}	
Effective Pore Area	A_{EFF}	d^2_{FMIN}/COLE	
Shape			
Bounding Box Width (mm)	W		Box drawn parallel to horizontal and vertical axes; Origin in upper left corner, so width may exceed height
Bounding Box Height (mm)	H		Box drawn parallel to horizontal and vertical axes; Origin in upper left corner, so width may exceed height
Roundness	R	$4A/(\pi*E_{MAJ}^2)$	Unitless
Aspect Ratio	AR	E_{MAJ}/E_{MIN}	Unitless
Tortuosity	T	(F)/(0.5*P)	Unitless
Solidity	S	A_{SSG} / Convex Hull Area	Unitless; Range 0-1 describing the roughness of the object
Orientation			
Feret Angle	F_A		Degree
Ellipse Angle	F_E		Degree
Abundance			
Number of SSGs	N		Count
SSG Density N/(mm2)	D_{SSG}	N/Axs	

3.2 Determination of soil properties that govern the expression of macropores across precipitation and land-use gradients

Spearman correlations were used to determine the relative correspondence between macropore geometry metrics and other soil properties. Relationships with an r critical value ≥ 0.40, as calculated using Bonferroni correction to account for familywise error rate were considered to have at least a moderate correlation between variables. Linear regression analysis was also performed to understand how changes in water fluxes and wetting-drying frequencies govern soil properties such as clay content, depth of the carbonate layers, rooting depth distributions, and soil organic carbon content; all of which have the potential to impact the geometry of macropores. Data

were first separated in the near surface (A, Ap, AB, and BA horizons) and subsurface horizons (B) and then analyzed by grouping data by overall MAP and land-cover type.

4 Results

4.1 Moisture Conditions across Sites

Kansas Mesonet precipitation data from 2018-2020 indicated that the frequency and the maximum intensity of precipitation events declined as site MAP decreased (Figure 3) similar to the long-term data (Section 2). During this time most sites received above-average precipitation when compared to the 30-year average. Hays recorded 775.4 mm in 2018 and 789.2 mm, in 2019, Manhattan (Konza) recorded 958.5 mm in 2018 and 1168.6 mm in 2019. Although Ottawa (Welda) recorded 916.9 mm in 2018, which was below the 30-year average, it received 1611.1 mm in 2019, which was well above average. A seasonal effect also emerged at each site, where warmer months showed the majority of intense precipitation events throughout the year.

The soil moisture records (10, 40, and 120 cm deep) at Konza started in October of 2018, while these same measurements were not monitored until the summer of 2019 for Hays and Welda. Direct comparisons between sites only focus on the time period when all sensors were collecting data. Moving across the precipitation gradient from driest to wettest (Hays to Welda) the behavior at the native sites showed that overall soil moisture increased when moving east, where moisture content at Hays was lower and differences in soil moisture content with depth were similar as compared to the other two sites. The largest magnitude of change in moisture content was observed at Konza, which tended to occur at 40 cm in the Native and Post-Agricultural land uses. Large magnitudes of change were observed for the Native and Post-Agricultural land uses at Welda. The Hays and Konza Agriculture land uses showed that soil moisture rapidly responded with depth, as compared to Welda, which showed more gradual changes in soil moisture over time. The soil moisture behavior at Post-Agricultural land use behaved similar to the Native land use, except at Welda the overall moisture content was lower and at Konza and Welda the signal was more dampened. Overall, soil moisture conditions at Konza appeared to undergo a greater degree of wetting and drying events compared to Welda and Hays, though Welda Native showed a large degree of these events with the signal progressively dampening as land-use intensity increased.

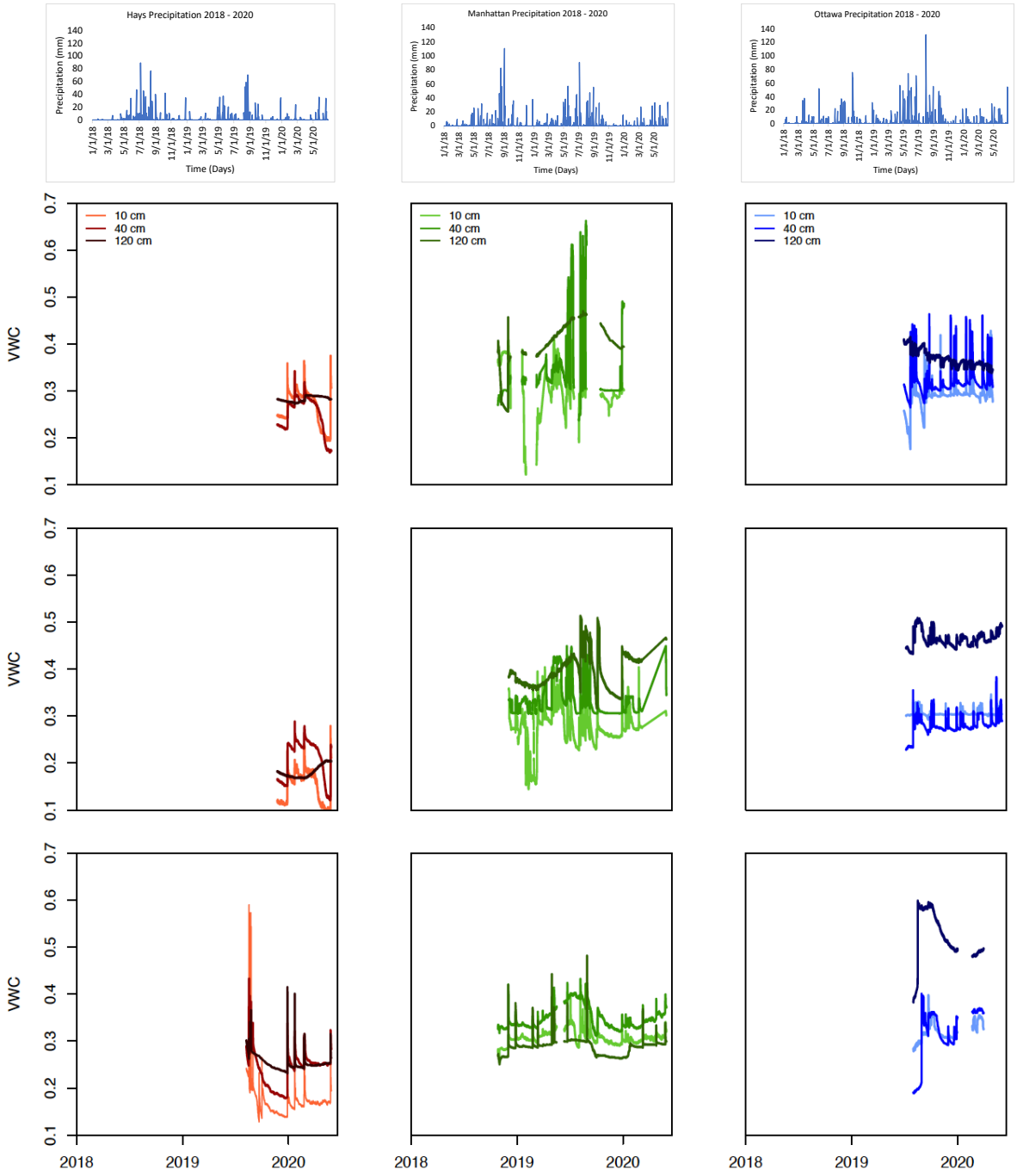

Figure 3 – Precipitation data (Mesonet) from January 2018 – June 2020 for Hays, Konza, and Welda (top row: left to right, respectively) compared to volumetric water content (VWC) for Hays, Konza, and Welda (left to right, respectively) for the Native (2nd row), Post-Ag (3rd row), and Agricultural (4th row). Soil moisture color darken with depth (10, 40, 120 cm).

4.2 Soil Profile Properties

Tables 3.1 – 3.3 show the NRCS descriptions of each soil pit, where horizon depths, texture class, structure, dry consistence, roots, pores, and carbonate morphology were classified. This information is useful for connecting soil properties to macropore properties across land use and precipitation gradients. Soil horizon descriptions revealed that the thickness of the A horizons systematically changed across the precipitation gradients, but in inverse ways for the Native and Agriculture land uses (Figure 4). Specifically, for Native and Post Agricultural land uses, A horizons were thickest at the driest site (Hays) and thinnest at the wettest site (Welda), while the opposite held true for the Agricultural land uses). Depth to Bt horizons, which indicates the translocation of clay into the B horizon, decreased with drying conditions at the Agricultural land uses only (i.e., shallowest at Hays and deepest at Welda). Interestingly, Hays was the only site that showed a shallowing of the Bt horizon with increased disturbance (i.e., shallowest at Agricultural and deepest at Native). The presence of carbonates in Bt horizons (Btk) were also observed to deepen with increased MAP. At Konza and Hays, the depth of carbonates became shallower at Agriculture land uses. Conversely, slickenside abundance, which indicates the presence of shrink-swell clays, increased with greater MAP regardless of land use (i.e., the cumulative thicknesses from all three pits at Welda and Konza were 296 cm and 279 cm, respectively, while slickenside expression was absent at Hays). Based on Btk horizons observed at Hays and slickenside horizons observed at Welda, the overall picture that emerges from these descriptions is that soil development varies across the Kansas precipitation gradient with carbonates potentially reflecting climatic controls on soil structure in dry conditions, and shrink-swell behavior reflecting climatic controls on soil structure in wetter conditions.

Tables 3.1 – 3.3 – showing pit descriptions of soils across MAP and land use gradients

Table 3.1.1

Horizon	Depth (cm)	Boundary	Munsell Color		Texture	Structure	Dry Consistence	Surface Features	Roots	Pores	Effervesence Class	$CaCO_3$ Morphology	Comments
			Dry	Moist									
Pit: Hays NPT													
A	0-39	clear-smooth	10YR 3/2	10YR 2/2	sicl	moderate fine granular	friable		common fine/ common very-fine		non		
BA	39-58	clear-smooth	10YR 4/2	10YR 3/2	sic	moderate medium subangular blocky/ moderate fine granular	firm		common fine/ common very-fine	common very-fine	non		
Bt	58-92	clear-smooth	10YR 4/2	10YR 3/2	sicl	strong fine subangular blocky/ weak medium prismatic	firm	65% clay films	common very-fine	common very-fine	non		
Btk1	92-112	clear-smooth	10YR 5/2	10YR 4/2	sicl	weak medium prismatic/ strong medium prismatic	firm	70% clay films on vertical ped faces	common very-fine	common fine/ common very-fine	non	5% fine threadlike carbonate masses	
Btk2	112-134	clear-smooth	10YR 5/3	10YR 4/3	sic	weak coarse prismatic/ strong medium prismatic	firm	80% clay films	common very-fine	common very-fine	non	5% fine threadlike carbonate masses/ 2% medium spherical weakly cemented carbonate concretions	
Btk3	134-174	clear-smooth	10YR 6/4	10YR 5/3	sic	moderate coarse prismatic/ moderate medium prismatic	firm	70% clay films		common very-fine	non	3% fine threadlike carbonate masses/ 5% medium spherical weakly cemented carbonate concretions	
Btk4	174-192	clear-smooth	7.5YR 5/4	7.5YR 4/4	sicl	moderate coarse prismatic/ moderate medium prismatic	firm	50% clay films		common very-fine	non	2% carbonate coats/ 2% fine threadlike carbonate masses/ 5% medium irregular carbonate masses/ 2% medium spherical weakly cemented carbonate concretions	
Btk5	192-206	abrupt-smooth	7.5YR 6/4	7.5YR 5/4		weak very coarse prismatic/ moderate medium prismatic	friable	3% clay films		common fine/ common very-fine	strong	10% carbonate coats/ 2% fine threadlike carbonate masses/ 4% medium irregular weakly cemented carbonate nodues	

Table 3.1.2

Horizon	Depth (cm)	Boundary	Munsell Color		Texture	Structure	Dry Consistence	Surface Features	Roots	Pores	Effervesence Class	$CaCO_3$ Morphology	Comments
			Dry	Moist									
Pit: Hays PPT													
Ap	0-15	abrupt-smooth	10YR 3/1	10YR 2/1	sicl	moderate fine-granular	friable		common fine/ common very-fine		non		
A	15-30	clear-smooth	10YR 4/2	10YR 3/2	sicl	weak medium subangular blocky/ fine-granular	firm		common fine/ common very-fine		non		
Bt	30-52	clear-smooth	10YR 5/3	10YR 4/3	sicl	moderate medium subangular blocky	firm	45% clay films	common very-fine	common fine/ common very-fine	non		
Btk1	52-68	clear-smooth	10YR 5/2	10YR 4/2	sicl	moderate medium prismatic/ moderate medium subangular blocky	firm	60% clay films	common very-fine	common very-fine	strong	3% fine carbonate threadlike masses	
Btk2	68-90	clear-wavy	7.5YR 5/2	7.5YR 4/2	sicl	moderate medium prismatic/ moderate medium subangular blocky	firm	45% clay films	common very-fine	common fine/ common very-fine	strong	3% carbonate coats/ 3% medium threadlike carbonate masses	
Btk3	90-141	gradual-smooth	7.5YR 5/4	7.5YR 4/4	sicl	moderate coarse prismatic/ moderate medium prismatic	firm	35% clay films	common very-fine	common fine/ common very-fine	strong	4% carbonate masses/ 4% spherical weakly-cemented carbonate concretions/ 2% weakly-	
Btk4	141-179	clear-smooth	10YR 6/4	10YR 5/4	sicl	moderate coarse prismatic	firm	3% clay films	common very-fine	common fine/ common very-fine	violent	6% fine irregular carbonate masses/ 2% fine irregular carbonate masses	
Btk5	179-216	clear-smooth	10YR 6/4	10YR 5/4	sil	moderate coarse prismatic	friable	1% clay films	common very-fine	common fine/ common very-fine	violent	2% fine threadlike carbonate masses/ 5% medium irregular weakly cemented cabonate nodules	

Table 3.1.3

Horizon	Depth (cm)	Boundary	Munsell Color		Texture	Structure	Dry Consistence	Surface Features	Roots	Pores	Effervesence Class	$CaCO_3$ Morphology	Comments
			Dry	Moist									
Pit: Hays APT													
Ap	0-17	abrupt-smooth	10YR 3/1	10YR 2/1	sicl	weak medium subangular blocky/ moderate fine granular	friable		common fine/ common very-fine		non		
BA	17-24	abrupt-smooth	10YR 4/2	10YR 3/2	sic	moderate medium subangular blocky/ moderate fine granular	firm		common fine/ common very-fine	common fine	non		
Bt1	24-46	gradual-smooth	10YR 5/2	10YR 4/2	sic	moderate medium subangular blocky	firm	30% clay films	common very-fine	common fine/ common very-fine	non		
Bt2	46-64	clear-smooth	10YR 5/3	10YR 4/3	sicl	weak medium prismatic/ strong medium subangular blocky	firm	60% clay films	common very-fine	common very-fine	non		
Btk1	64-75	abrupt-wavy	7.5YR 6/4	7.5YR 5/4	sicl	weak medium prismatic/ moderate medium subangular blocky	firm	45% clay films	common very-fine	common fine/ common very-fine	non	1% fine threadlike carbonate masses	
Btk2	75-92	clear-smooth	10YR 7/4	10YR 6/4	sicl	weak coarse prismatic/ moderate medium prismatic	friable	30% clay films	common very-fine	common fine/ common very-fine	strong	5% carbonate coats on vertical faces/ 2% medium irregular carbonate masses/ 5% medium spherical weakly cemented carbonate concretions	
Btk3	92-130	gradual-smooth	10YR 6/4	10YR 5/4	sicl	weak coarse prismatic/ moderate medium prismatic	friable	4% clay films		common fine/ common very-fine	strong	3% carbonate coats/ 4% fine irregular weakly cemented carbonate nodules/ 3% medium irregular carbonate masses	
Btk4	130-180	gradual-smooth	10YR 7/4	10YR 6/4	sicl	weak coarse prismatic/ weak medium prismatic	friable	4% clay films		common fine/ common very-fine	strong	1% fine irregular carbonate masses/ 2% fine threadlike carbonate masses/ 2% medium irregular weakly cemented carbonate nodules	
Btk5	180-210		10YR 6/4	10YR 5/4	cl	weak very coarse prismatic/ moderate medium prismatic	friable	2% clay films		many very-fine	strong	2% medium threadlike carbonate masses	

Table 3.2.1

Horizon	Depth (cm)	Boundary	Munsell Color		Texture	Structure	Dry Consistence	Surface Features	Roots	Pores	Effervesence Class	$CaCO_3$ Morphology	Comments
			Dry	Moist									
Pit: Konza NPT													
A1	0-15	clear-smooth		10YR 2/2	sicl	moderate medium granular	friable		common fine/ many medium	many fine dendritic tubular	non		
A2	15-29	clear-smooth		10YR 2/1	sicl	moderate medium granular	friable		many fine roots	common fine dendritic tubular	non		
Bt1	29-59	clear-smooth		10YR 3/2	sic	weak medium prismatic/ moderate medium subangular	very-firm	25% clay films	common very-fine	common fine dendritic tubular	non		
Bt2	59-86	clear-wavy		10YR 4/3	sic	weak medium prismatic/ moderate medium subangular	very-firm	30% clay films	common very-fine	common fine dendritic tubular	non		
Btk1	86-127	clear-wavy		10YR 4/4	sic	weak medium prismatic/ moderate medium subangular	very-firm	25% clay films	common very-fine	common very-fine dendritic tubular	non		
Btk2	127-179	clear-wavy		10YR 5/4	sic	weak medium prismatic/ moderate medium subangular	firm	20% clay films/ 2% fine spherical masses of oxidized iron with clear boundaries	common very-fine	common very-fine dendritic tubular	non	35% coarse irregular moderately cemented 10YR 8/1 carbonate concretions with sharp boundaries	
2Bt	179-200			7.5YR 4/4	sic	weak medium prismatic/ moderate medium subangular	friable	25% clay films/ 5% coarse spherical masses of oxidized iron with clear boundaries/ 2% non-flat subangular indurated 2-5 mm chert fragments	common very-fine	common very-fine dendritic tubular	non	15% coarse irregular moderately cemented 10YR 8/1 carbonate concretions with sharp boundaries	

Table 3.2.2

Horizon	Depth (cm)	Boundary	Munsell Color		Texture	Structure	Dry Consistence	Surface Features	Roots	Pores	Effervesence Class	$CaCO_3$ Morphology	Comments
			Dry	Moist									
Pit: Konza PPT													
Ap1	0-11	abrupt-smooth		10YR 2/1	sicl	strong fine granular	very-friable		many fine		non		
Ap2	11-22	clear-smooth		10YR 2/1	sicl	moderate medium subangular blocky	friable		many fine		non		
Bt	22-68	clear-wavy		10YR 2/1	sic	moderate medium prismatic/ moderate medium subangular blocky	very-firm	40% clay films	common fine	common fine dendritic tubular	non		
Btss1	68-103	clear-wavy		10YR 2/1	sic	moderate medium prismatic/ moderate medium subangular blocky	very-firm	40% clay films/ 35% slickensides	common very-fine	common fine dendritic tubular	non		
Btss2	103-135	clear-wavy		10YR 3/1	sic	moderate medium prismatic/ moderate medium angular blocky	very-firm	50% clay films/ 30% slickensides	common very-fine	common fine dendritic tubular	non		
Btkss	135-175	clear-wavy		10YR 3/2	sic	moderate medium prismatic/ moderate medium angular blocky	very-firm	40% clay films/ 20% slickensides	common very-fine	common fine dendritic tubular	non	1% fine irregular moderately cemented 10YR 8/1 carbonate nodules with sharp boundaries/ 3% very-fine prominent irregular 10YR 8/1 carbonate masses with diffuse boundaries	
2Btky	175-200			10YR 3/2	sic	moderate medium prismatic/ moderate medium angular blocky	firm	40% clay films/ 1% fine irregular 10YR 8/1 gypsum masses with diffuse boundaries		common fine dendritic tubular	very-slight	5% fine irregular 10YR 8/1 carbonate masses with diffuse boundaries	

Table 3.2.3

Horizon	Depth (cm)	Boundary	Munsell Color		Texture	Structure	Dry Consistence	Surface Features	Roots	Pores	Effervesence Class	$CaCO_3$ Morphology	Comments
			Dry	Moist									
Pit: Konza APT													
Ap1	0-15	abrupt-smooth		10YR 2/1	sicl	moderate thin platy	friable		common very-fine		non		
Ap2	15-26	abrupt-smooth		10YR 2/1	sic	moderate medium angular blocky	firm		common very-fine		non		
Bt	26-47	clear-smooth		10YR 2/1	sic	weak medium prismatic/ moderate medium subangular blocky	firm	40% clay films	common very-fine	many fine dendritic tubular	non		
Btss	47-71	clear-smooth		2.5Y 3/1	sic	moderate medium prismatic/ moderate medium subangular blocky	firm	40% clay films/ 15% slickensides	common very-fine	many fine dendritic tubular	slight		
Btkss1	71-113	gradual-smooth		10YR 3/2	sic	moderate medium prismatic/ moderate medium angular blocky	very-firm	40% clay films/ 10% slickensides	common very-fine	many fine dendritic tubular	slight	3% fine irregular 10YR 8/1 carbonate masses with clear boundaries	
Btkss2	113-139	clear-smooth		10YR 3/2	sic	moderate medium prismatic/ moderate medium angular blocky	very-firm	50% clay films/ 10% slickensides	common very-fine	many fine dendritic tubular	strong	5% fine irregular 10YR 8/1 carbonate masses with clear boundaries	
Btkss3	139-194	clear-smooth		10YR 3/2	sic	moderate medium prismatic/ moderate medium subangular blocky	firm	50% clay films/ 20% slickensides	common very-fine	many fine dendritic tubular	strong	5% fine irregular 10YR 8/1 carbonate masses with clear boundaries	
Btkss4	194-200			10YR 3/2	sic	moderate medium prismatic/ moderate medium subangular blocky	firm	50% clay films/ 10% slickensides		common fine dendritic tubular	strong	3% fine irregular 10YR 8/1 carbonate masses with diffuse boundaries	

Table 3.3.1

Horizon	Depth (cm)	Boundary	Munsell Color		Texture	Structure	Dry Consistence	Surface Features	Roots	Pores	Effervesence Class	Comments
			Dry	Moist								
Pit: Welda NPT												
A	0-19	clear-wavy		10YR 2/2	sil	weak fine granular	very-friable	2% non-flat indurated 2-75 mm chert fragments	common medium/ many very-fine	many very-fine dendritic tubular	non	
AB	19-37	abrupt-wavy		10YR 2/2	gr-sicl	weak fine granular	friable	25% non-flat indurated 2-75 mm chert fragments	common medium/ many very-fine	many very-fine dendritic tubular	non	
2Bt	37-64	abrupt-wavy		10YR 4/2	grx-sil	weak fine subangular blocky	friable	15% 7.5YR 4/4 clay films/ 80% non-flat subrounded indurated 2-75 mm chert fragments/	many very-fine	common very-fine dendritic tubular	non	
2E	64-82	abrupt-wavy		10YR 6/3		weak very-fine subangular blocky	friable	3% fine irregular 5YR 4/6 masses of oxidized iron with clear boundaries/ 90% non-flat subrounded indurated 2-75 mm chert fragments	common very-fine	common very-fine dendritic tubular	non	
2B't	82-129	abrupt-wavy		10YR 5/6	grv-c	weak very-fine subangular blocky	friable	40% 7.5YR 5/1 clay films/ 15% fine irregular 2.5YR 4/6 masses of oxidized iron with clear boundaries/ 50% non-flat subrounded indurated 2-75mm chert fragments/		common very-fine dendritic tubular	non	
3BCss	129-167	abrupt-wavy		60% 10YR 6/6/ 40% 2.5Y 6/2	c	weak fine angular blocky	firm	60% slickensides/ 3% fine irregular 5YR 4/6 masses of oxidized iron with clear boundaries on root channels/ 5% medium irregular 10YR 2/1 iron-manganese masses with clear boundaries			non	
3Cr	167-200			80% 5Y 6/2/ 20% 10YR 6/6	c	structureless platy	friable	60% slickensides/ 2% fine irregular 5YR 4/6 masses of oxidized iron with clear boundaries on root channels/ 2% medium irregular 10YR 2/1iron-manganese masses with clear boundaries			non	

Table 3.3.2

Horizon	Depth (cm)	Boundary	Munsell Color		Texture	Structure	Dry Consistence	Surface Features	Roots	Pores	Effervescence Class	Comments
			Dry	Moist								
Pit: Weldo PPT												
Ap	0-7	clear-smooth		10YR 3/1	sil	moderate fine subangular blocky	very-friable	2% non-flat subrounded indurated 2-5 mm chert fragments	common fine/ common medium	many very-fine dendritic tubular	non	
AB	7-22	clear-smooth		10YR 3/1	sicl	moderate medium subangular blocky/ moderate fine angular blocky	friable	25% pressure faces/ 3% non-flat subrounded indurated 2-5 mm chert fragments	common fine/ common very-fine	many very-fine dendritic tubular	non	
2Bt1	22-38	clear-smooth		70% 10YR 3/2/ 30% 7.5YR 4/3	sicl	weak fine prismatic/ moderate medium subangular blocky	friable	20% 7.5YR 4/4 clay films/ 2% fine irregular 7.5YR 5/6 masses of oxidized iron with clear boundaries/ 3% very fine faint irregular 10YR 2/1 iron-manganese masses with clear boundaries/ 3% non-flat subrounded indurated 2-5 mm chert fragments	common fine/ common very-fine	common very-fine dendritic tubular	non	
2Bt2	38-55	clear-smooth		7.5YR 4/3	sic	moderate fine prismatic/ moderate medium subangular blocky	friable	25% 7.5YR 5/3 clay films/ 1% medium faint irregular 7.5YR 5/3 oxidized masses of iron with clear boundaries/ 2% fine distinct irregular 10YR 2/1 iron-manganese masses with clear boundaries/ 2% very-fine distinct irregular iron-mangenese masses with clear boundaries/ 3% very-fine irregular 7.5YR 4/6 masses of oxidized iron with clear boundaries/ 3% non-flat subrounded indurated 2-5 mm chert fragments	common very-fine	common very-fine dendritic tubular	non	
2Bt3	55-91	abrupt-wavy		7.5YR 4/1	sic	moderate fine prismatic/ moderate medium subangular blocky	friable	55% 7.5YR 5/1 clay films/ 1% medium distinct irregular 10YR 2/1 iron-manganese masses with clear boundaries/ 2% medium irregular 5YR 4/4 masses of oxidized iron with clear boundaries/ 2% very-fine irregular 2.5YR 4/6 masses of oxidized iron with clear boundaries/ 40% non-flat subrounded indurated 2-5 mm chert fragments	common very-fine	common very-fine dendritic tubular	non	
2Btss	91-118	clear-smooth		7.5YR 5/4	sic	moderate fine prismatic/ moderate medium wedge	firm	5% 10YR 2/1 organoargillans along pores/ 60% 7.5YR 6/4 clay films/ 15% slickensides/ 1% medium distinct irregular 5YR 4/6 masses of oxidized iron with clear boundaries/ 2% distinct irregular 10YR 6/2 masses of reduced iron with clear boundaries/ 2% fine irregular 5YR 4/6 masses of oxidized iron with clear boundaries/ 2% very-fine irregular weakly cemented 10YR 2/1 iron-manganese nodules with clear boundaries/ 2% medium 10YR 5/1 masses of reduced iron with clear boundaries/ 3% fine irregular 10YR 2/1 iron-manganese masses with clear boundaries	common very-fine	common very-fine dendritic tubular	non	
3Btkss	118-168	abrupt-wavy		7.5YR 5/6	grv-sic	moderate medium prismatic/ moderate medium wedge	very-firm	5% 10YR 2/1 organoargillans along pores/ 45% 7.5YR 6/4 clay films/ 30% slickensides/ 2% fine irregular 10YR 6/2 masses of reduced iron with clear boundaries/ 3% very-fine irregular 10YR 2/1 iron-manganese masses with clear boundaries/ 3% spherical strongly-cemented 10YR 8/1 carbonate nodules with sharp boundaries/ 3% medium spherical 10YR 8/1 carbonate nodules with sharp boundaries	common very-fine	common very-fine dendritic tubular	non	
3Btss	168-191	abrupt-wavy		7.5YR 5/8	c	strong medium prismatic/ moderate medium wedge	firm	5% 10YR 2/1 organoargillans along pores/ 40% 7.5YR 4/3 clay films/ 40% slickensides/ 1% medium irregular 10YR 2/1 iron-manganese masses with clear boundaries/ 2% fine irregular weakly-cemented 10YR 2/1 iron-manganese nodules with clear boundaries		common very-fine dendritic tubular	non	
3R	191-200											

Table 3.3.3

Horizon	Depth (cm)	Boundary	Munsell Color		Texture	Structure	Dry Consistence	Surface Features	Roots	Pores	Effervescence Class	Comments
			Dry	Moist								
Pit: Welda APT												
Ap1	0-15	abrupt-wavy		10YR 2/1	sil	weak coarse platy/ weak fine subangular blocky/ weak coarse platy/ weak medium subangular blocky	friable		common very-fine	many medium dendritic tubular	non	
Ap2	15-36	abrupt-wavy		10YR 2/1	sil	weak coarse platy/ weak medium subangular blocky	friable		common very-fine	many fine dendritic tubular	non	
AB	36-50	abrupt-wavy		10YR 2/1	sicl	moderate medium subangular blocky	firm		common very-fine	common fine dendritic tubular	non	
2Bt	50-75	clear-wavy		10YR 2/1	sicl	moderate medium subangular blocky	very-firm	1% very-fine spherical 10YR 3/3 masses of oxidized iron with clear boundaries	common very-fine	common fine dendritic tubular	non	
2Btss	75-121	clear-wavy		2.5Y 3/1	sicl	moderate medium prismatic/ moderate medium subangular blocky	very-firm	5% 10YR 2/1 organoargillans along pores/ 5% percent slickensides/ 50% 2.5Y 3/2 clay films/ 3% fine distinct irregular 10YR manganese masses with clear boundaries/ 10% very-fine irregular 2.5Y 5/4 masses of oxidized iron with diffuse boundaries/ 2% fine irregular 10YR 8/1 gypsum masses with diffuse boundaries in matrix/ 2% non-flat rounded indurated 2 to 5-millimeter chert fragments	common very-fine	common very-fine dendritic tubular	non	
2Btssyg	121-152	gradual-wavy		2.5Y 4/2	sicl	moderate medium prismatic/ moderate medium subangular blocky	very-firm	5% 10YR 2/1 organoargillans along pores/ 5% slickensides/ 50% 2.5Y clay films/ 3% fine irregular 10YR 2/1 manganese masses with clear boundaries/ 10% very-fine irregular 2.5Y 5/4 masses of oxidized iron with diffuse boundaries/ 2% fine irregular 10YR 8/1 gypsum masses with diffuse boundaries in matrix/ 2% non-flat rounded indurated 2 to 5-millimeter chert fragments	common very-fine	common very-fine dendritic tubular	non	
3Btkg1	152-173	clear-wavy		2.5Y 5/2	sicl	weak medium prismatic/ moderate medium subangular blocky	firm	30% 2.5Y 4/2 clay films/ 3% very-fine irregular 10YR 2/1 manganese masses with clear boundaries/ 40% medium faint irregular 2.5Y 5/3 masses of oxidized iron with diffuse boundaries/ 3% medium irregular 10YR 8/1 carbonate masses with diffuse boundaries/ 2% non-flat rounded indurated 2 to 5-millimeter chert fragments	common very-fine	common very-fine dendritic tubular	non	
3Btkg2	173-200			2.5Y 5/2	sicl	weak medium prismatic/ moderate medium subangular blocky	firm	30% 10YR 5/1 slickensides/ 3% very-fine irregular 10YR 2/1 iron-manganese masses with clear boundaries/ 45% medium irregular 7.5YR 4/6 and 10YR 6/6 masses of oxidized iron with diffuse boundaries/ 2% fine irregular 10YR 8/1 carbonate masses with diffuse boundaries/ 2% non-flat rounded indurated 2 to 5-millimeter chert fragments	common very-fine	common very-fine dendritic tubular	non	

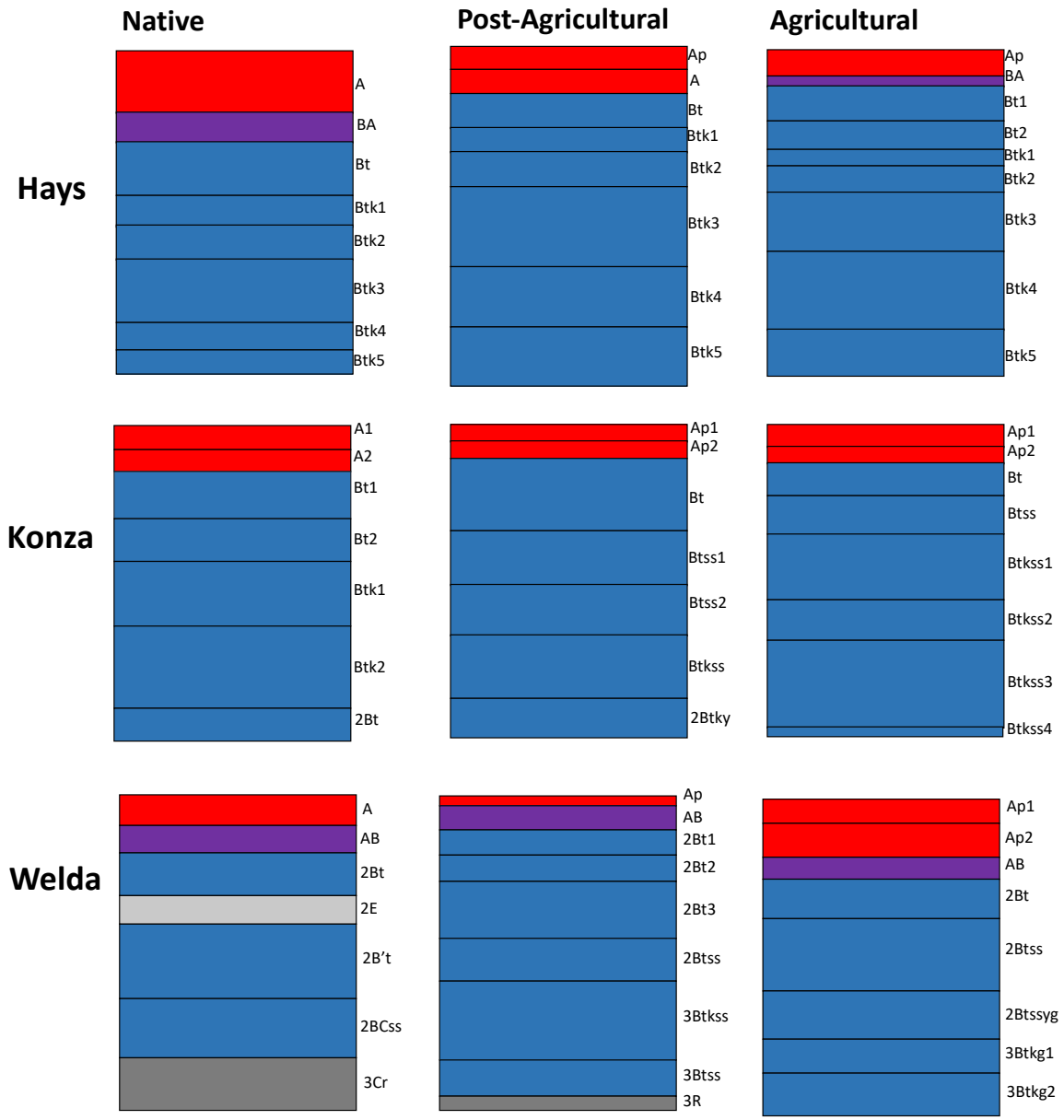

Figure 4 – Comparison of NRCS soil profile descriptions, with red representing topsoil (A) horizons, purple representing transition (AB, BA) horizons and blue representing subsoil (B) horizons.

Soil structure, as described by the NRCS, also changed across the sites (Figure 5). Generally, surface soils are more granular or subangular blocky, and become more prismatic or angular blocky with depth. Some structural features vary with climate, such as more prevalent prismatic structure at the Hays and Konza sites and wedge structure observed at Welda. We also observed

differences across land use for the depths at which these structural properties were expressed. For example, the Hays sites expressed prismatic structures within more shallow depths at more intensively managed land uses (Agricultural) than lesser ones (Native), with the Post-Agricultural site falling in between. A similar trend was noticed across the MAP gradient, where the prevalence of granular structure diminished, and was replaced by a surface platy structure at the Agricultural land uses at Konza and Welda. Similar to horizon thickening at the Agricultural land uses with MAP (Figure 4), soil structure also changed with an increase in the thickness of platy structure and decreased width of granular structure (Figure 5).

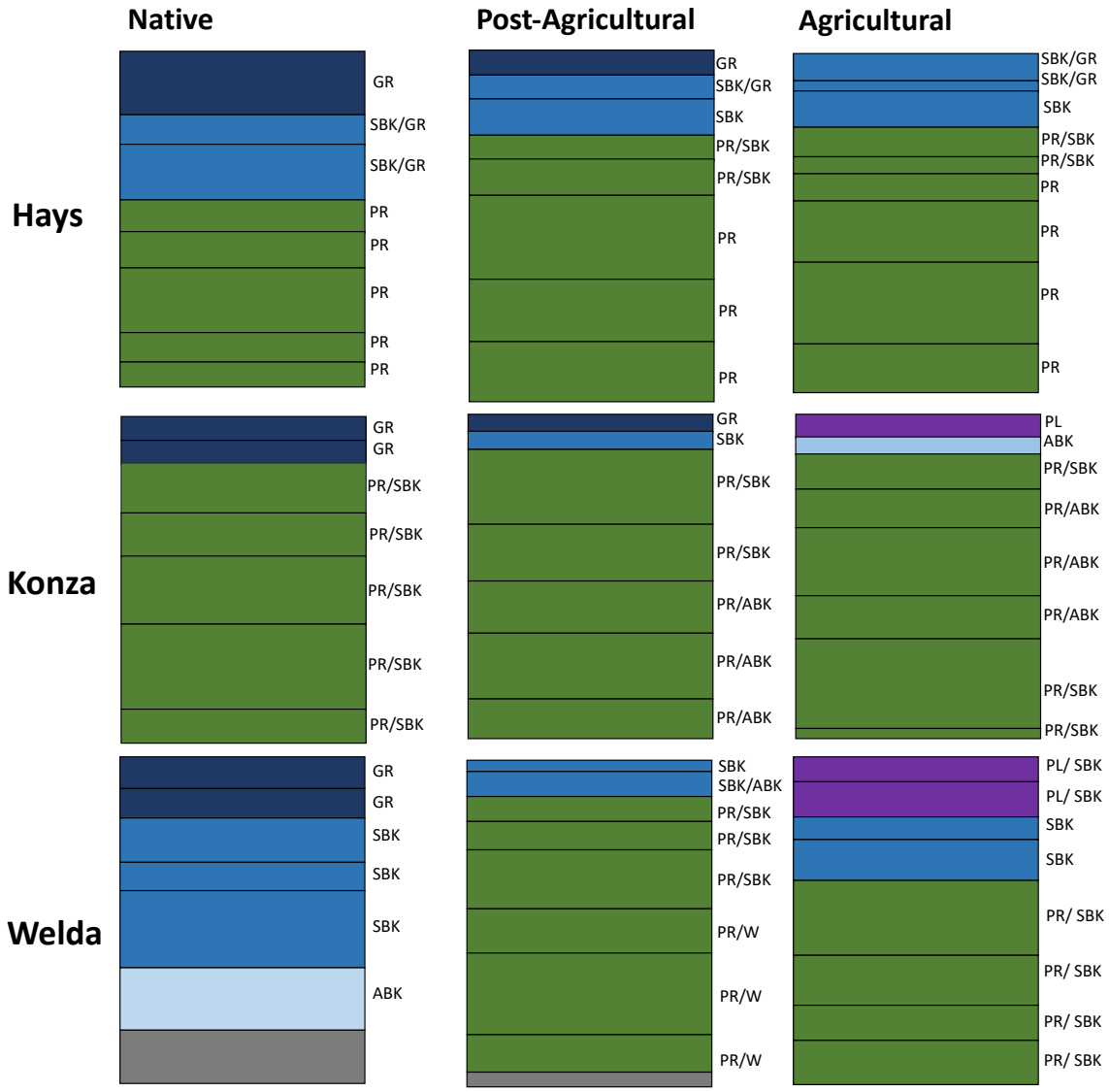

Figure 5 - Comparison of soil structure as described by the NRCS, where purple = platy-dominant, dark blue = granular-dominant, blue = subangular blocky-dominant, light blue = angular-blocky dominant, green = prismatic-dominant, and grey = bedrock.

Descriptions of parent material and depth to bedrock also differed between sites. It is important to note that our interpretations of trends across the precipitation gradient can be confounded by the parent material complexities at Welda Native and Post-Agricultural land uses, as a result we often emphasize differences between Hays and Konza over comparison at all three sites in the Native/Post-Ag land uses. At Hays the parent material was identified as loess and the depth to bedrock was not reached. At Konza the parent material was identified as alluvium (Post-Ag and Agricultural), which is also likely re-worked loess through alluvial processes, or alluvium over colluvium (Native) and the depth to bedrock was also not observed at the bottom of the pit, though the underlying lithology is known to be an interbedding of limestone and shale layers (Wehmueller, 1996). At Welda the parent material was identified as re-worked loess over colluviated alluvium over residuum for Post-Ag and Native land uses, and the depth to bedrock was observed at 191 cm and 167 cm, respectively.

Quantitative measures of soil properties also showed differences across the precipitation and land use gradients (Table 3). When examining the overall pedon mean depth-weighted differences between land uses, the data showed that as precipitation increased: 1) clay content, particles < 0.002 mm in size, increased, while the sand content, particles 0.1 - 2.0 mm in size, declined (i.e., values were more elevated at Hays compared to Konza and Welda), 2) estimated organic carbon content (EOC) increased, similar to the total, fine root, and coarse root densities (Table 1; Souza et al. Prep), and 3) COLE, field capacity, and wilting point increased, while porosity decreased. Interestingly, the saturated hydraulic conductivity of the matrix soil (K_{sm}) determined from many of these properties showed the lowest values at Konza and the highest values at Welda, followed by Hays (Table 3).

Table 3 – Depth-weighted mean soil properties for three lands uses (Native, Post-Ag, and row-crop Agriculture) across the Kansas precipitation gradient (dry to wet: Hays, Konza, Welda).

	Hays			Konza			Welda		
	Native	Post-Agriculture	Agriculture	Native	Post-Agriculture	Agriculture	Native	Post-Agriculture	Agriculture
Clay (%)	37.9 +/- 5.2	33.0 +/- 4.8	36.4 +/- 4.8	43.8 +/- 6.6	46.9 +/- 5.3	41.2 +/- 0.9	52.1 +/- 20.8	50.8 +/- 11.2	41.6 +/- 9.9
Silt (%)	51.3 +/- 3.8	51.6 +/- 3.8	48.1 +/- 1.6	51.5 +/- 5.2	49.8 +/- 4.5	51.7 +/- 0.9	36.1 +/- 19.6	44.5 +/- 10.2	54.7 +/- 9.3
Sand (%)	10.8 +/- 2.4	15.4 +/- 5.3	15.5 +/- 4.2	4.7 +/- 2.0	3.3 +/- 1.2	7.1 +/- 1.0	11.8 +/- 6.9	4.7 +/- 1.2	3.7 +/- 1.8
EOC (%)	0.7 +/- 0.6	0.5 +/- 0.8	0.3 +/- 0.4	0.8 +/- 0.9	1.1 +/- 0.7	0.6 +/- 0.4	0.8 +/- 1.2	0.6 +/- 0.6	1.0 +/- 0.8
COLE (cm^3/cm^3)	0.04 +/- NA	0.04 +/- 0.01	0.03 +/- 0.02	0.07/ +/- 0.02	0.07 +/- 0.02	0.05 +/- 0.01	0.07 +/- NA	0.1 +/- 0.04	0.08 +/- 0.03
Porosity (%)	37.8 +/- NA	37.2 +/- 1.6	39.6 +/- 5.0	32.2 +/- 7.3	28.1 +/- 2.8	30.6 +/- 2.1	32.5 +/- NA	30.4 +/- 8.4	32.0 +/- 6.5
Bulk Density (g/cm^3)	1.6 +/- NA	1.6 +/- 0.04	1.6 +/- 0.1	1.7 +/- 0.2	1.8 +/- 0.07	1.8 +/- 0.05	1.7 +/- NA	1.8 +/- 0.2	1.7 +/- 0.2
Field Capacity (%)	24.2 +/- NA	22.8 +/- 2.0	21.1 +/- 2.3	26.9 +/- 3.0	25.8 +/- 2.4	21.8 +/- 1.8	30.3 +/- NA	29.1 +/- 6.9	28.4 +/- 1.7
Wilting Point (%)	15.3 +/- 1.9	13.8 +/- 2.7	15.7 +/- 2.0	19.1 +/- 2.3	19.6 +/- 2.0	16.6 +/- 0.9	18.9 +/- 6.4	20.3 +/- 5.5	18.2 +/- 3.5
K_{sm} (µm/s)	10.8 +/- 1.7	11.2 +/- 0.7	14.1 +/- 1.4	12.1 +/- 1.3	4.0 +/- 0.2	5.3 +/- 0.3	19.9 +/- 4.0	15.5 +/- 1.1	10.2 +/- 0.5

When the soils were divided into the near surface horizons (A, AP, AB, and BA) and subsurface horizons (B) sand, EOC and total roots shows similar patterns for both depths across sites (Figure 6 and 7), while clay, silt, and EOC showed patterns reversed in the near surface horizons compared to the subsurface horizons. Specifically, in the surface horizons clay content and COLE declined with increased MAP, while silt content increased.

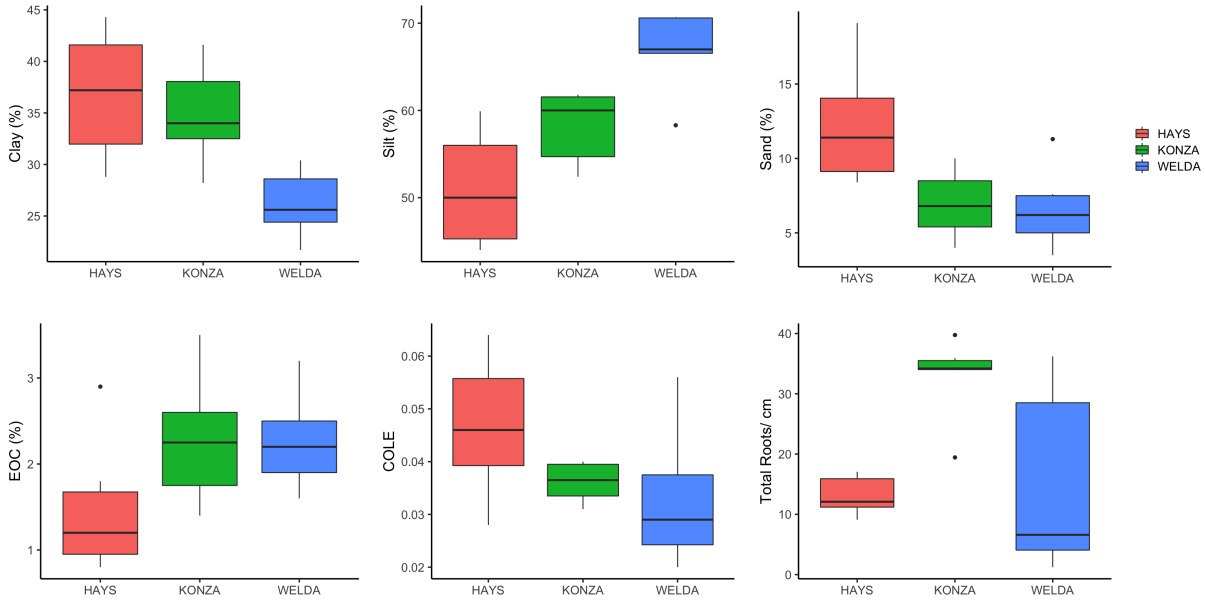

Figure 6 - Boxplots for A horizons of the soil texture (clay, silt, sand; top row left to right, respectively), and estimated organic carbon (EOC), confidently of linear extensibility (COLE; measure of shrink-swell) and mean root abundance for Hays (red), Konza (green), and Welda (blue).

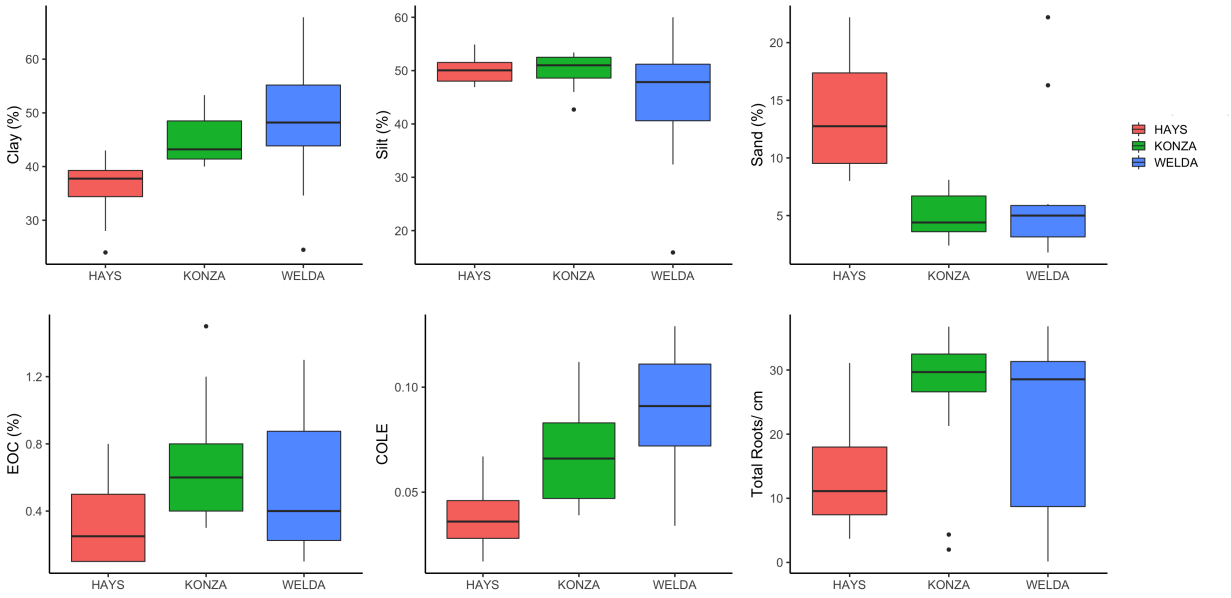

Figure 7 – Boxplots for B horizons of the soil texture (clay, silt, sand; top row left to right, respectively) , and estimated organic carbon (EOC), confidently of linear extensibility (COLE; measure of shrink-swell) and mean root abundance for Hays (red), Konza (green), and Welda (blue).

4.3 Macropore properties

4.3.1 Overall trends across precipitation and land use gradients: Depth weighted-mean of properties

We focused on the pedon scale macropore properties using depth-weighted means across land uses (Table 4) and distribution of the data (Figures 8 and 9). Native land uses were first analyzed, as they represent a control for how soil pore behavior should naturally vary across the Kansas precipitation gradient. As MAP increased at Native land uses, pore angle increased while Aeff decreased. Interestingly, the depth-weighted mean properties at Konza was often higher than the Hays and Welda land uses, particularly for the mean area, perimeter, Feret diameter, and minimum Feret diameter metrics. Tortuosity coefficients were similar across each site.

Macropores were compared in the Native land uses to data from Agricultural and Post-Agricultural settings. Metrics such as pore minor axis, Feret angle, minimum Feret diameter, tortuosity coefficient, aspect ratio, Macropore density (Dssg) – the number of pores per given area of soil, fraction (ssgF) – the fractional area of the macropore to the total cross-sectional area of the soil, and effective pore area (Aeff) – the square of the minimum Feret diameter divided by the

coefficient of linear extensibility - generally followed the same direction despite land use. The strength of metric expression, in many cases, were lower for soils that experienced more intensive land-use practices.

When we compared the Agricultural land uses to the Native land uses we found that all sites expressed an increase in aspect ratio (and, thus, a decrease in roundness) and a decrease in macropore density. At Konza and Welda the major axis, mean Feret diameter, and solidity increased, while tortuosity coefficients only increased at Welda. In comparison, macropore fraction decreased. A decrease in macropore metrics was also observed at both the wettest and driest sites, where pore perimeter was highest at Konza and pore angle was highest at Welda, and declined across the MAP gradient.

Figures (8 and 9) show that mean aspect ratio and tortuosity coefficients were higher at Agricultural than Native land uses for both the near surface (A horizons) and subsurface (B horizons) within soils, but this trend diminished when moving toward drier MAP sites. Additionally, Agricultural compared to Native land use showed a lower pore density in the subsurface horizons, which suggest fewer avenues for water flow and possibly more rapid saturation after precipitation events. It is not clear whether Post-Agricultural settings reverse these trends across all sites, as some macropore metrics differed substantially from Native land use in wetter conditions (e.g., macropore density in A horizons and mean aspect ratio and tortuosity coefficients in B horizons at Welda), while other differences were expressed in drier conditions (e.g., mean macropore area and perimeter in A horizons at Hays). Properties also differed between A and B horizons, where pore area and perimeter showed a more elevated values in A horizons than B horizons when comparing the Agricultural and Native land uses.

Table 4 - Depth-weighted means and standard deviations of macropore properties across all pits sampled.

	Hays			Konza			Welda		
	Native	Post-Agriculture	Agriculture	Native	Post-Agriculture	Agriculture	Native	Post-Agriculture	Agriculture
Mean Area (mm^2)	7.2 +/- 0.5	7.4 +/- 1.1	7.0 +/- 1.0	7.2 +/- 0.9	9.4 +/- 2.9	9.4 +/- 2.6	7.4 +/- 1.0	7.2 +/- 1.6	8.3 +/- 1.0
Mean Perimeter (mm)	26.3 +/- 0.7	26.8 +/- 2.7	26.6 +/- 2.7	27.9 +/- 3.2	31.9 +/- 5.4	32.0 +/- 5.8	26.2 +/- 2.6	26.1 +/- 2.8	27.0 +/- 3.0
Mean Width (mm)	5.6 +/- 0.6	5.7 +/- 0.4	6.1 +/- 0.5	5.8 +/- 0.5	6.6 +/- 0.9	6.6 +/- 1.2	6.2 +/- 0.8	5.5 +/- 0.7	6.4 +/- 1.0
Mean Height (mm)	5.0 +/- 0.4	5.2 +/- 0.8	4.7 +/- 0.6	5.5 +/- 0.7	6.1 +/- 1.2	5.8 +/- 1.0	4.5 +/- 0.3	5.4 +/- 0.6	4.8 +/- 0.4
Mean Feret Diameter (mm)	7.9 +/- 0.4	8.2 +/- 0.8	8.3 +/- 0.8	8.3 +/- 0.8	9.6 +/- 1.4	9.9 +/- 1.6	7.7 +/- 0.8	7.8 +/- 0.9	8.5 +/- 0.9
Mean Min Feret Diameter (mm)	3.0 +/- 1.0	3.0 +/- 0.4	2.8 +/- 0.3	3.2 +/- 0.4	3.3 +/- 0.5	3.2 +/- 0.4	3.0 +/- 0.2	3.0 +/- 0.2	2.8 +/- 0.3
Mean Feret Angle	62.8 +/- 10.3	57.0 +/- 13.1	64.1 +/- 10.1	73.0 +/- 13.6	65.7 +/- 8.2	63.6 +/- 9.4	66.4 +/- 16.2	71.2 +/- 14.0	61.4 +/- 14.0
Mean Pore Angle	64.1 +/- 13.9	54.2 +/- 10.8	55.4 +/- 9.7	59.0 +/- 15.5	68.6 +/- 14.0	54.9 +/- 6.5	64.1 +/- 21.5	68.0 +/- 16.3	54.2 +/- 12.1
Mean Tortuosity	0.61 +/- 0.02	0.62 +/- 0.04	0.64 +/- 0.03	0.61 +/- 0.04	0.62 +/- 0.03	0.64 +/- 0.03	0.60 +/- 0.04	0.61 +/- 0.03	0.64 +/- 0.03
Mean Aspect Ratio	3.2 +/- 0.2	3.4 +/- 0.6	3.7 +/- 0.5	3.3 +/- 0.5	3.7 +/- 0.5	4.0 +/- 0.6	3.1 +/- 0.5	3.1 +/- 0.3	3.8 +/- 0.4
Mean Roundness	0.35 +/- 0.03	0.34 +/- 0.05	0.32 +/- 0.04	0.34 +/- 0.05	0.32 +/- 0.03	0.29 +/- 0.05	0.37 +/- 0.05	0.37 +/- 0.03	0.31 +/- 0.03
Mean Solidity	0.45 +/- 0.01	0.44 +/- 0.03	0.43 +/- 0.03	0.41 +/- 0.03	0.42 +/- 0.01	0.44 +/- 0.02	0.46 +/- 0.04	0.44 +/- 0.03	0.49 +/- 0.03
Arel	0.06 +/- 0.01	0.05 +/- 0.03	0.04 +/- 0.01	0.06 +/- 0.05	0.06 +/- 0.01	0.05 +/- 0.03	0.05 +/- 0.02	0.05 +/- 0.04	0.03 +/- 0.01
Aeff	246.8 +/- NA	238.6 +/- 67.4	313.4 +/- 130.2	167.0 +/- 91.8	161.3 +/- 75.0	224.7 +/- 80.0	140.0 +/- NA	145.3 +/- 137.9	128.6 +/- 93.0

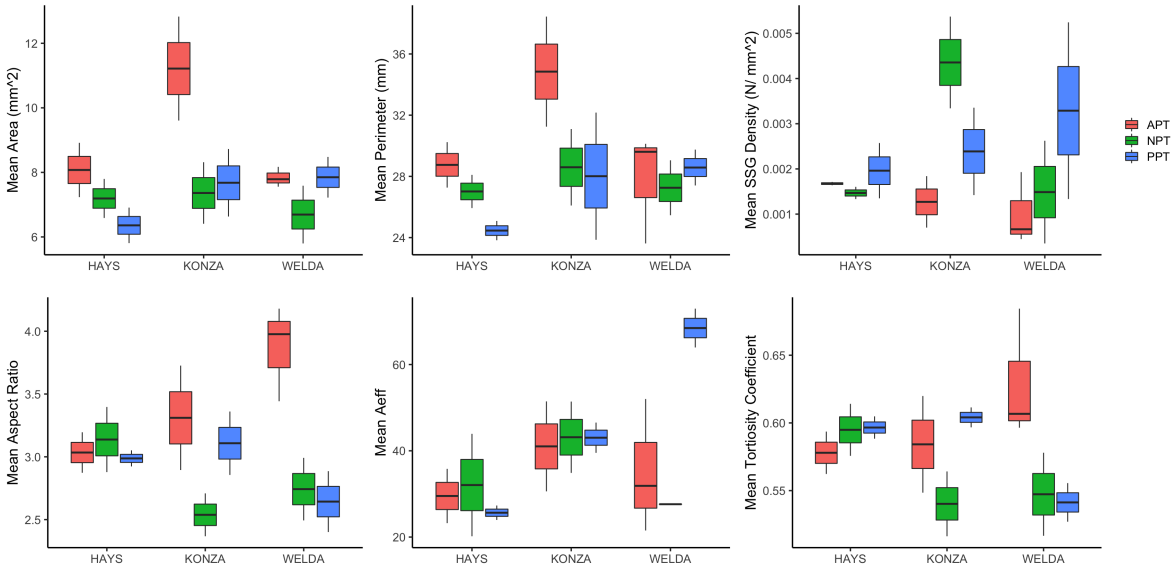

Figure 8 - Boxplots for near surface horizons (A, Ap, AB, and BA) of key macropore metrics (mean area, perimeter, and Dssg; top row left to right and mean aspect ratio, Aeff, and tortuosity coefficients; bottom row left to right), for Agriculture (red), Native (green), and Post-Agricultural (blue) land uses.

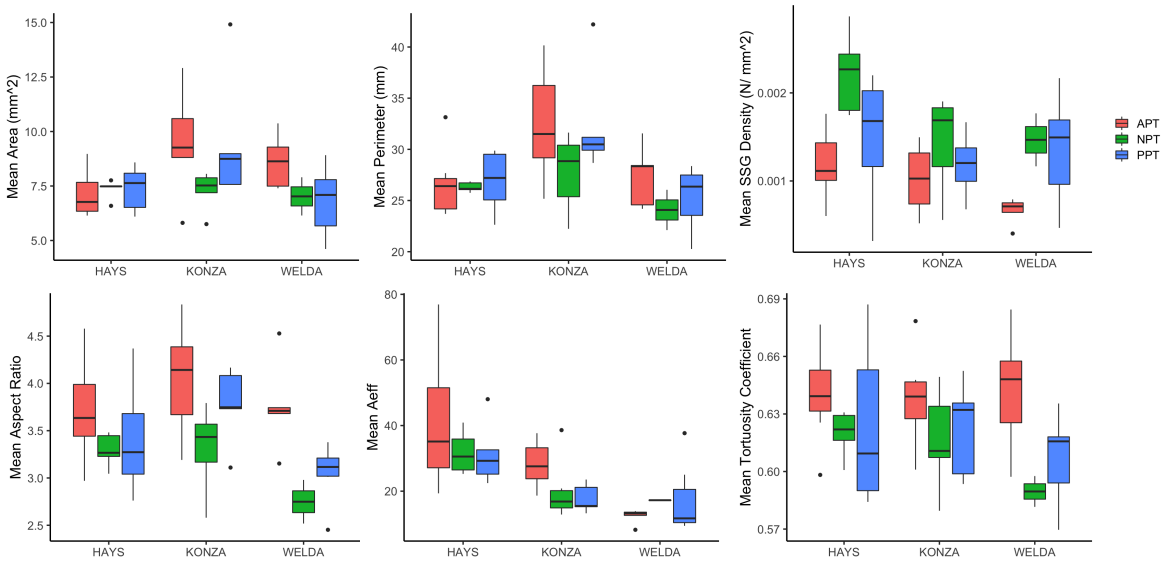

Figure 9 – Boxplots for B horizons of key macropore metrics (mean area, perimeter, and Dssg; top row left to right and mean aspect ratio, Aeff, and tortuosity coefficients; bottom row left to right), for Agriculture (red), Native (green), and Post-Agricultural (blue) land uses.

4.3.2 Effect of soil development and depth: Variation of macropore properties with depth

Soil properties often change with depth due to the accumulation of translocated clays (Mohammed et al., 2020) and carbonates that can significantly alter the structural geometries of peds and, thus, pores. To address this, we examined how macropore properties change with soil properties across depth to gain insight on the effect of development and depth. Across all Native land uses we observed that the aspect ratio and tortuosity coefficient (values near 1 indicate very straight pores) increased with depth; while Dssg decreased with depth at Konza and Welda, but increased at Hays (Figure 10). Macropores at Konza and Welda were more similar with depth compared Hays, here we observed that at greater depths there was an increase in Feret angle, while pore area, perimeter, pore angle, minimum Feret diameter and macropore fraction decreased with depth. Some macropores at Hays behaved similarly with depth to either Konza or Welda but not both. Specifically, Hays and Welda both showed an increased Feret diameter with depth.

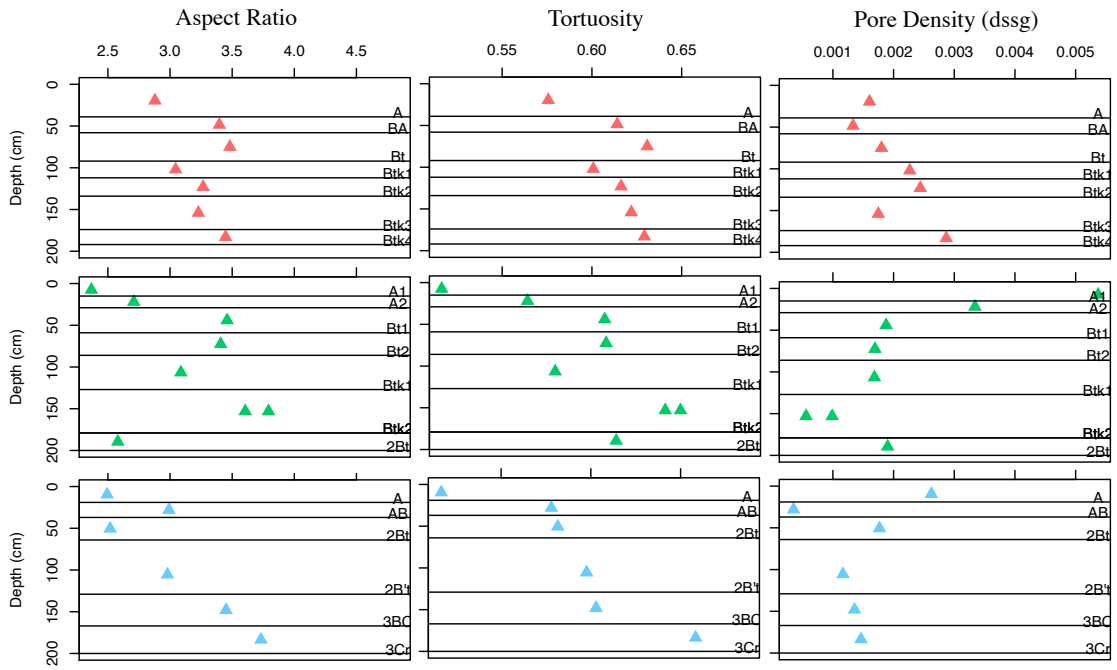

Figure 10 – Comparison of mean aspect ratio, tortuosity coefficient, and macropore density across Native land uses with depth between Hays (red), Konza (green), and Hays (blue) sites.

We then compared changes in depth with differing land use the to examine the degree to which depth relationships changed (strengthening or weakening, as determined by the direction of the trend relative to the horizon above) by the overall moisture condition (wetter vs. drier sites). Thus, macropore patterns with depth often would be shared by two sites (e.g., Hay and Konza) but not by the third site. At Native land uses, many of the macropore metrics had strong relationships with depth including a decrease in pore roundness, and an increase in tortuosity coefficient, aspect ratio, and solidity. Although Native land uses did not show a clear trend for pore area with depth, Agricultural land uses showed a strong decrease. Both Native and Agricultural land uses showed decreases in minor axis length, minimum Feret diameter, roundness, and ssgF, along with a consistent increase in tortuosity coefficient. The relationship of minimum Feret diameter strengthened at Agricultural land uses for Konza and Welda.

Post-Agricultural land uses were also compared to Native land uses with depth, which showed strong decreasing relationships with depth for pore minor axis, roundness, Dssg, and Aeff along with increases for aspect ratio, and size, where Welda and Konza land uses were more similar to

each other than Hays. Some metrics switched at Konza and Welda, as solidity shifted from an increase to decrease at both sites. Pore angle was consistent across sites.

The overall message that emerges across all sites is the pathway upon which water flows becomes straighter as the density of pores declines with depth into the subsurface. In addition, the data suggest that the precipitation difference between Hays and Konza may provide a controlling threshold in moisture conditions, whereby similar hydrologic conditions at Konza and Welda support the development of similar macropore characteristics with depth. This may suggest that increasing land disturbance can potentially lead to greater decreases for macropores such as minimum Feret diameter and macropore fractional area.

4.3.3 Macropore Variation with Pore Angle Orientation

Given that pore angle plays a critical role in water flow, we also examined macropores with respect to angle. We divided pore angle into three categories: horizontal (0 - 20 degrees), angled (20 - 70 degrees), and vertical (70 - 90 degrees) orientation (Figure 11). When we examined the depth-weighted means at Native land uses, we observed differences in how the area, perimeter, and Feret diameter of vertical pores declined with a decrease in MAP. The perimeter of angled pores also followed this trend. As angle increased at Konza the solidity decreased. The density of pores consistently declined with lower MAP for both horizontal and vertical pores, but not angled pores. Hays and Konza showed with a decrease in Aeff with an increased angle at Hays and vise-versa for Konza. These trends with angle differed as depth increases across the precipitation gradient, where we observed that pore angle at the Native land uses followed a more linear trend in wetter environments than drier ones, particularly for pore area, perimeter, major axis length, Feret diameter, and aspect ratio. Conversely, angle may follow more linear trends for pore circularity in drier environments than the wetter ones. Some metrics, such as and pore size followed similar trends at the wet and dry sites, but there was no apparent effect at Konza, the central site.

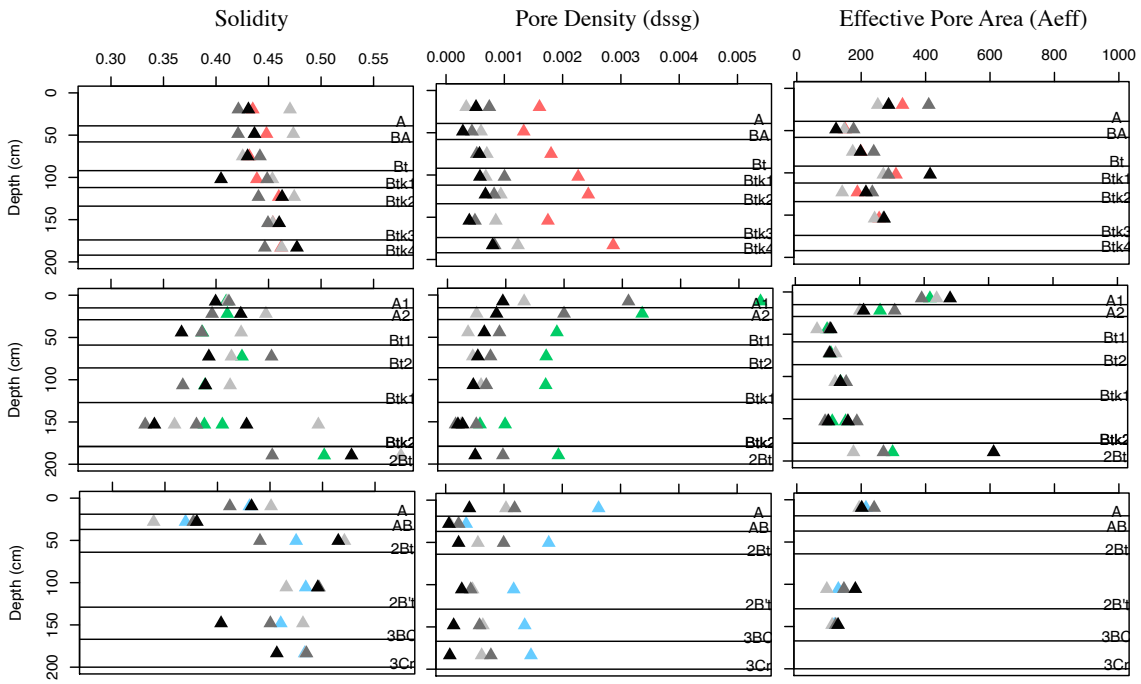

Figure 11 – Depth profiles of pore solidity (left), density (Dssg; center), and effective pore area (Aeff; right) for the Native land uses at Hays (top, red), Konza (middle, green), and Welda (bottom, blue) land uses. Mean values for angle classes are expressed through shades of gray, where light gray represents horizontal pores (0 - 20 degrees), medium gray represent angled pores (20 - 70 degrees), and dark gray represents vertical pores (70 - 90 degrees). Color represent the mean of all pores together.

Similar to Native land uses, changes in angle across Agricultural land uses showed that pore area, perimeter, and Feret diameter also declined in vertical pores as MAP increased; perimeter of angled pores showed a similar declining trend. Figure 12 shows that solidity at the Agricultural land uses showed the same pattern at Konza but increased with angle at Hays, while the density of pores generally declined with increased angle. A clear relationship with the Agricultural land uses was not observed with MAP, like the Native land uses. At the Agricultural land uses, Aeff only diverged for vertical pores, with Konza showing substantially greater values than Hays.

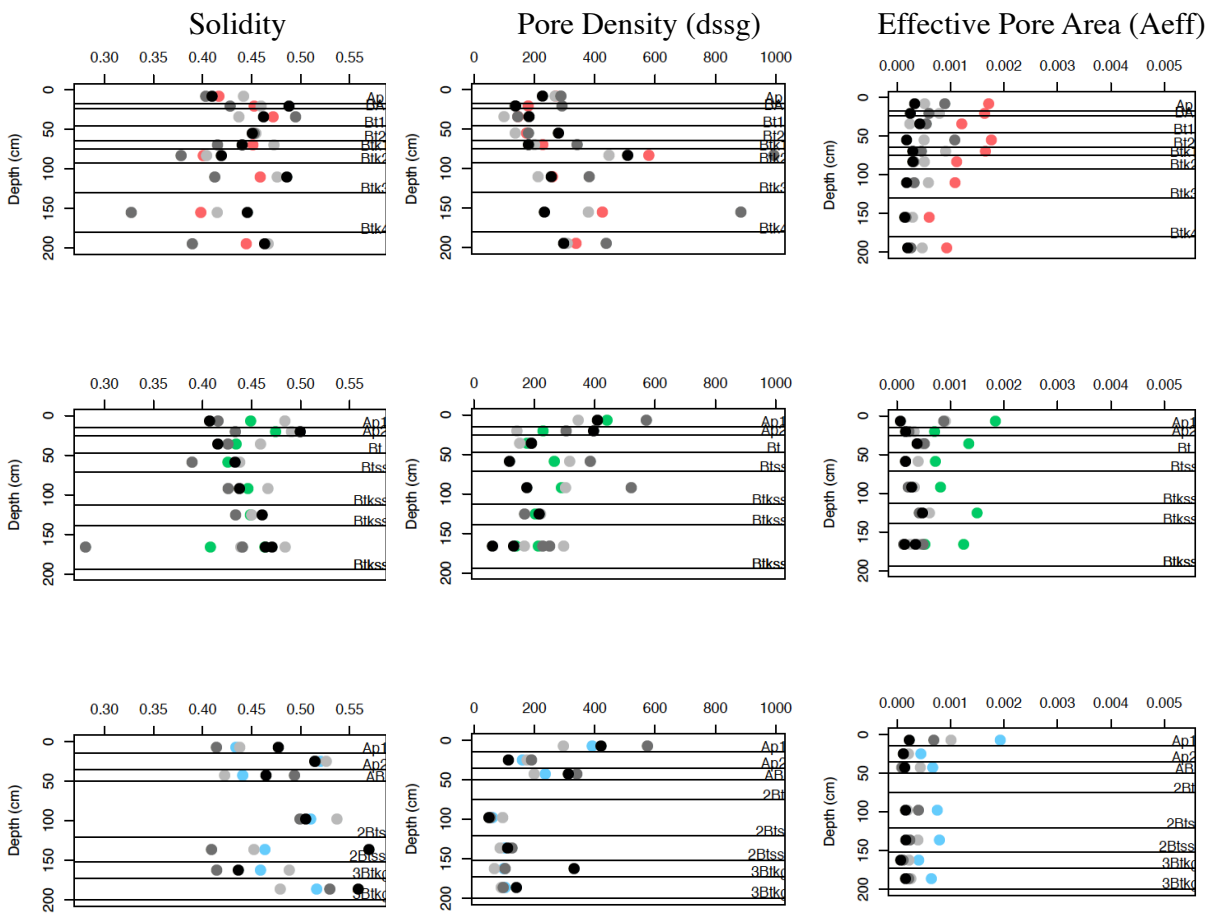

Figure 12 – Depth profiles of pore solidity (left), density (Dssg; center), and effective pore area (Aeff; right) for the Agricultural land uses at Hays (top, red), Konza (middle, green), and Welda (bottom, blue) land uses. Mean values for angle classes are expressed through shades of gray, where light gray represents horizontal pores (0 - 20 degrees), medium gray represent angled pores (20 - 70 degrees), and dark gray represents vertical pores (70 - 90 degrees). Color represent the mean of all pores together.

We compared angle at the Native land uses to Post-Agricultural land uses. Post-Agricultural land uses showed a decline in angled pores for pore perimeter and minimum Feret diameter. Similar to the Native land uses, Aeff at the Post-Agricultural land uses declined for Hays and increased at Konza (Figure 13). The Post-Agricultural land use also showed a negative trend with angle at deeper horizons for minimum Feret diameter, which contrasted with a positive relationship at the Native land use. Overall, relationships of macropores with angle appeared to show the strongest trends at the Post-Agricultural land use when compared to the Native land use at Konza. Pore area and perimeter increased with angle at the surface and decreased in deeper horizons. Many pore metrics lost a clear connection with angle at the Post-Agricultural land use when compared

to the Welda Native land use. Some examples include pore area, perimeter, major axis, and Feret diameter, and minimum Feret diameter, which switched the direction of the trend, where it increased with angle and depth at the Native land use, but decreased with angle and depth at the Post-Agricultural land.

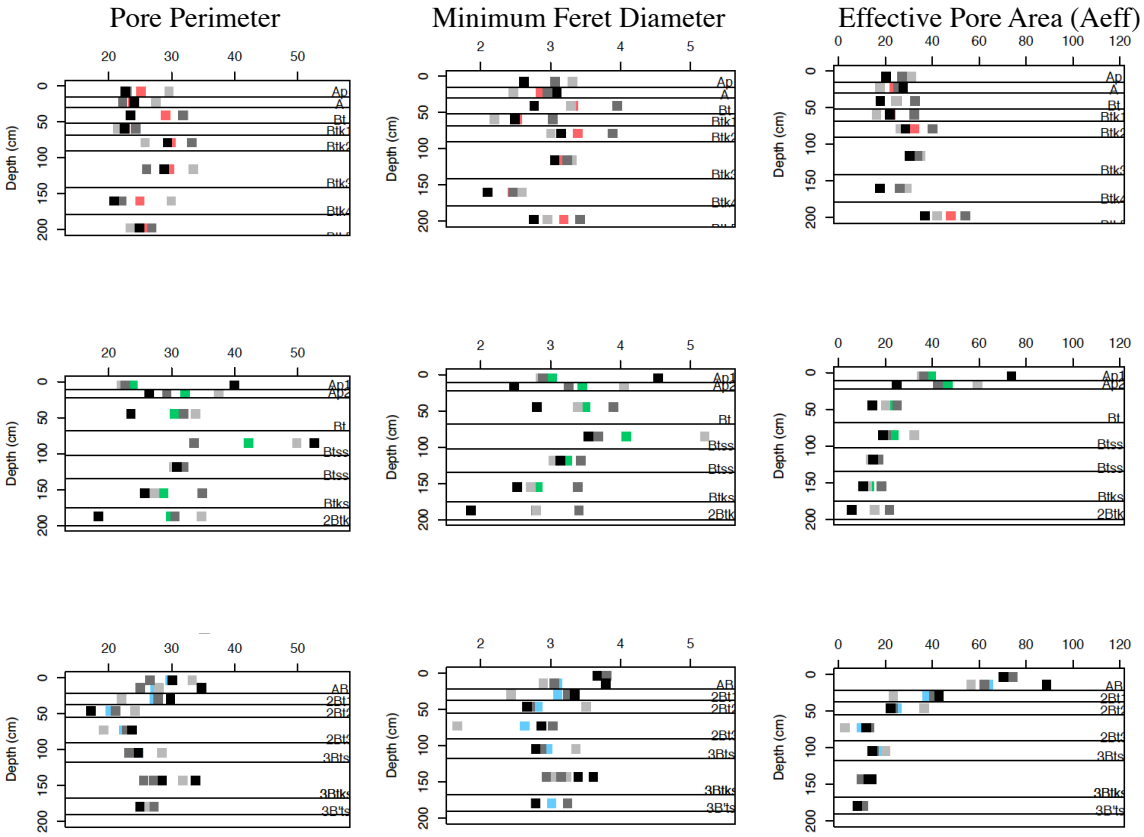

Figure 13 – Depth profiles of pore perimeter (left), minimum Feret diameter (Dssg; center), and effective pore area (Aeff; right) for the Post-Agricultural land uses at Hays (top, red), Konza (middle, green), and Welda (bottom, blue) land uses. Mean values for angle classes are expressed through shades of gray, where light gray represents horizontal pores (0 - 20 degrees), medium gray represent angled pores (20 - 70 degrees), and dark gray represents vertical pores (70 - 90 degrees). Color represent the mean of all pores together.

4.4 Relationship between macropores and soil physical and chemical properties

After observing differences in pore metrics across precipitation, land use, depth, and angle, we further examined their relationships with soil physical and chemical properties, such as particle size distribution and EOC, using linear regressions near-surface horizons and subsurface horizons where a p-value threshold < 0.05 was used to determine significance of relationships.

4.4.1 Drivers of macropore properties across the MAP gradient

We examined these same relationships across the precipitation gradient, where we found negative relationships between clay percentage and Aeff, along with positive relationships between mean aspect ratio and depth for both A and B horizons. Some trends were specific to surface horizons, while others were specific to subsurface horizons. For example, a positive relationship was observed between mean pore density and EOC in A horizons (Figure 13), while a negative relationship was observed between EOC and mean tortuosity coefficient in B horizons (Figure 14).

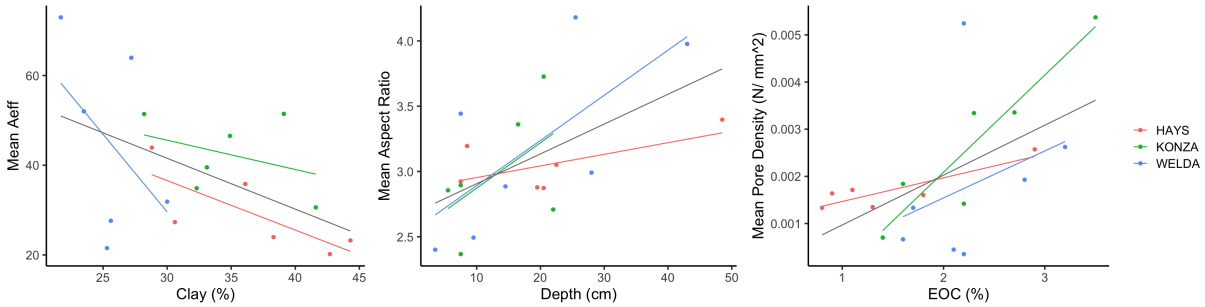

Figure 13 – Regressions for mean Aeff with percent clay (left), mean aspect ratio and depth (middle), and mean pore density with EOC (right), where the grey lines represent a significant relationship for all A horizons and the red (Hays), green (Konza), and blue (Welda) lines represent how the relationships deviate across the MAP gradient.

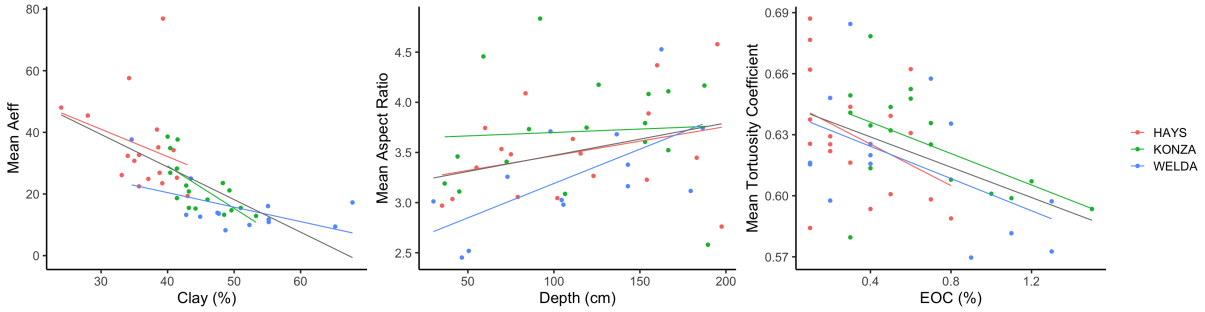

Figure 14 – Regressions for mean Aeff with percent clay (left), mean aspect ratio and depth (middle), and mean tortuosity coefficient with EOC (right), where the grey lines represent a significant relationship for all A horizons and the red (Hays), green (Konza), and blue (Welda) lines represent how the relationships deviate across the MAP gradient.

4.4.2 Drivers of macropore properties across land use

Native land uses overall expressed a higher number of strong relationships, using a correlation threshold > 0.40 between environmental drivers and macropores compared to Agricultural land uses (stronger colors top right corner of Figure 11). Compare Native and Ag sites for both A and B horizons.

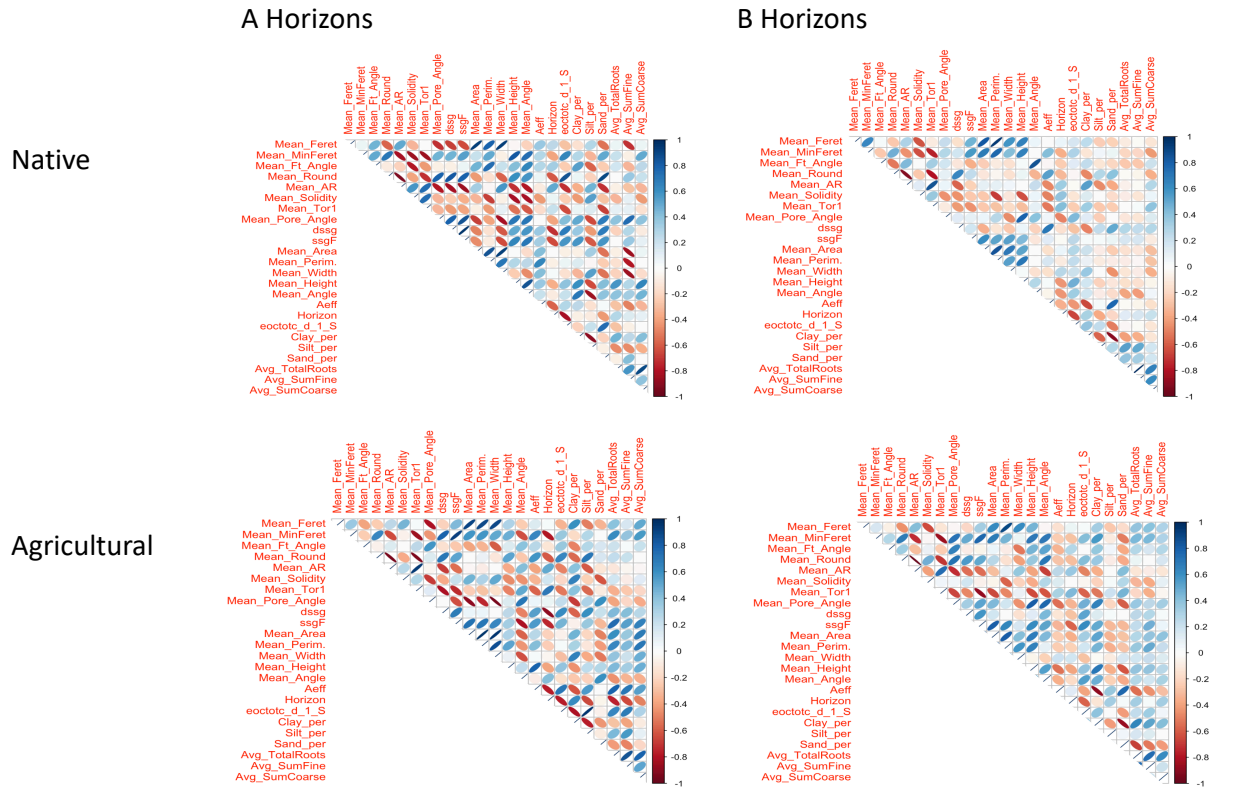

Figure 15- Correlation plots across a variety of macropores and environmental drivers and land use and between A and B horizons, where red ellipses are negative relationships and blue ellipses are positive relationships. More bold colors indicate stronger correlations.

To investigate differences in correlations across land use, we used linear regression to compare slopes, where the significance of the relationship found at Native land uses was lost for Feret diameter and roundness with clay percentage at the Agricultural land uses. Conversely, the relationship between pore solidity and percent sand was more significant at Agricultural land uses than Native land uses. There were far fewer correlation changes at the same correlation threshold between Native and Post-Agricultural land uses as opposed to the Agricultural land uses, suggesting that the systems in some way are responding more similarly to each other. Percent clay

was a particularly dynamic environmental driver across land usage, as shown in Figures 16 and 17.

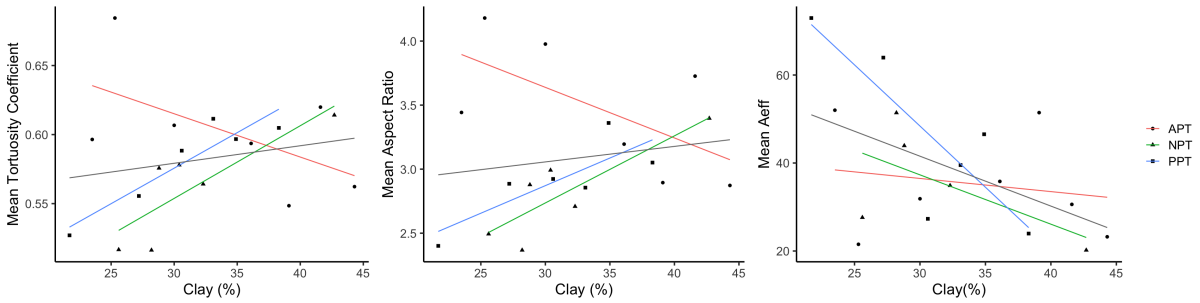

Figure 16 – Comparison for A horizons of macropore relationships with percent clay across land use; where strong correlations were observed between percent clay and mean tortuosity coefficient, aspect ratio, and Aeff.

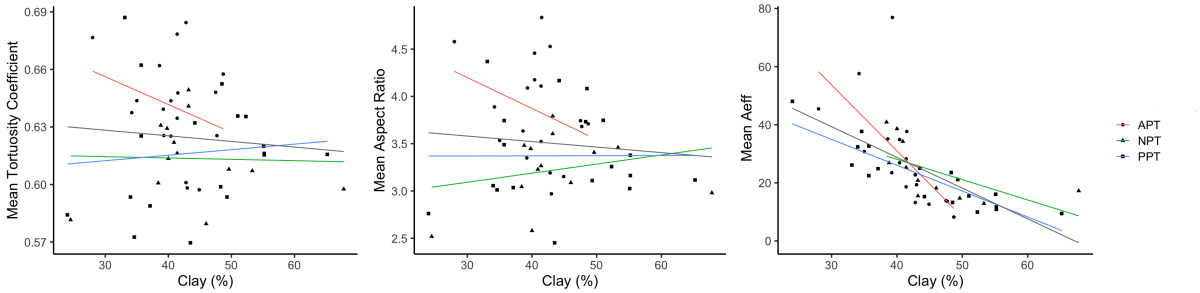

Figure 17 – Comparison for B horizons of macropore relationships with percent clay across land use; where Agricultural land uses showed the strongest correlations between tortuosity coefficient and aspect ratio with percent clay, and Aeff with percent silt.

5 Discussion

Soil macropore geometry was captured to ~1.9 m deep across precipitation and land use (e.g., Agriculture, Post-Agriculture, and Native) in Kansas and related to measurements of soil moisture and structure. These data indicate that meteoric precipitation and depth play strong and interactive roles controlling soil macropore geometry, and that agriculture can either dampen or even reverse the relationship between pore geometry metrics and environmental drivers (e.g., EOC and percent clay). Building off of evidence from Billings et al. (2018), our data also show that the influence of agriculture can influence soil functioning, through controls on soil macropore geometry, to much greater depths then are typically considered (~30 cm). Below we expand on these ideas and discuss their implications.

5.1 *Climate, particularly MAP, influences pore geometry*

We observed that pore geometry varied with MAP conditions. Specifically, we observed differences in regression trends, such as negative relationships between Aeff with percent clay for both A and B horizons at Hays, while showing reversed directions at Welda, when compared with Konza and Hays, between EOC and Aeff, where trends were negative in A horizons and positive in B horizons. Given the strong correlation of many of these metrics to particles size and EOC, which fined and increased, respectively, with greater inputs of precipitation, we infer that MAP plays an important role in governing macropore properties. While observed by qualitative methods, the variance in carbonate accumulation across sites (i.e., increasing with aridity) could depict a likely interaction that control the morphology of structure at depth (Figure 4). Here we observe stronger prismatic structure at shallower depths in the drier sites compared to the wetter sites where subangular blocky structure becomes more dominant at depth compared to prismatic structures (Figure 5). Interestingly, this difference in structure type corresponded to greater pore density and effective pore area (Aeff) with depth at the drier site (Hays) compared to the wetter sites (Konza and Welda). Differences in soil physical structure has been shown to vary with climate. Results from a recent continental-scale study of ~1600 pedons demonstrates ped shape and size are largely associated with climate (Mohammed et al., 2020). In dry and/or cold climates a greater abundance of large anisotropic peds occur, while humid and/or warm climates promote finer equidimensional peds. While our study does not span such a large range in climatic conditions, results show even a ~500 mm difference in MAP can govern variations is soil structure that persist down to ~2 m depth, and that these differences also manifest in the geometry of macropores.

Not only did clay content and slickenside prevalence – the amount of high-clay content pressure facies as represented by Btss horizons or wedge structure classification - increase with MAP, but so did COLE while minimum Feret diameter remain fairly constant across sites. The net effect of higher shrink-swell in soils, in relation to consistent minimum Feret diameter measurements, leads to a lower Aeff at wetter sites. More simply, it indicates that higher shrink-swell capacities as a result of greater clay contents at wetter sites, but not necessarily wider pores within their networks, result in more expanded aggregates and, thus, sealed pore spaces during precipitation events. Given observed positive linear relationships between Aeff and Ksat used by Eck et al. 2016, our

observations suggest Ksat declines with increased MAP, thus reducing groundwater recharge. Soil depth exerts strong controls on macropore properties.

Changes in ped structure influence the spaces of macropores, which directs the flow of water in the soil profile. Mohammed et al. (2020) shows that regardless of climate, overburden pressure may increase ped size in all environments, which was also observed across the three sites, where near surface granular and platy structure tended to be more dominant while prismatic and subangular blocky were more dominant at depth. Several macropore metrics showed strong relationships with depth across all sites and land use types. For example, the tortuosity coefficient and aspect ratio increased with depth at all sites, while the density of pores (Dssg) decreased. These data indicate a declining number of spaces for soil water flow at depth than at the surface, and that they are being routed along less tortuous flowpaths. Overall, Konza and Welda shared more similarities with macropores over depth than at Hays, which could point to a fundamental shift in macropore properties between the Konza and Hays sites. Specifically, greater decreases in minimum Feret diameter with depth indicate thinner pores at wetter sites, when combined with higher shrink-swell capacities, could significantly inhibit subsurface flow with depth when compared to drier conditions.

5.2 *Intensive land use alters macropore geometry*

When comparing Native to Agricultural land uses, stark differences persisted, some of which are expected near the surface, and others not so expected at depth. Specifically, root abundance (especially course roots) were lower at Agricultural land uses when compared to Native land uses. Additionally, topsoil thickness declined and/or transitioned from granular to platy structure. Such changes in topsoil, along with differences in EOC, are to be expected given tillage practices (Franzluebbers, 2002; Mohammed et al., 2020). The relationship between percent clay and the tortuosity coefficient and aspect ratio, as well as percent silt and Aeff strengthened under Agricultural land use. These data suggest that Agricultural practices may have profound impacts on macropore geometry at depths much greater the plowing, specifically it appears to create straighter pores that may support quicker drainage of the land.

5.3 Frequency of wetting and drying drives differences in soil response with depth

More frequent precipitation events were observed at Welda, and the occurrences declined when moving west. Native soils at Konza showed the greatest soil moisture response to precipitation

events, followed by Welda, then Hays. Native soils also showed more fluctuation than Agricultural soils, which expressed rapid increases and decreases in soil moisture, followed by periods of stable moisture conditions until the next precipitation event. Surface soils showed greater magnitude of responses to precipitation events than in the subsurface, which showed dampened, slower responses. Surficial pore structure varies at Agricultural land uses as opposed to Native land uses, where topsoil is either less thick or shows greater thicknesses of platy structure - differences that have implications for more compacted pores (Alvarez et al., 2014) and thus lower effective pore area.

6 Conclusion

Developing more quantitative means by which to link climate and land use to soil macropore distributions helps advance our understanding of how changing environmental conditions impact water resources (e.g., groundwater recharge and land-atmosphere exchange of latent heat). Here we compared differences in macropore geometry across the natural precipitation and land-use gradients of Kansas with depth (~2 m) across semi-arid (580 mm) to mesic (1080 mm) gradient of precipitation where temperature regimes are fairly similar. We examined the difference between Native and Agricultural land uses, while examining Post-Agricultural land uses to understand the potential recovery of soil macropore distributions toward more Native conditions. Here we extracted small soil monoliths spanning ~2 m deep from nine pits across these gradients and installed soil moisture sensors. We scanned soil monoliths with the multistripe triangulation scanning method at 0.18 mm resolution and derived pore metrics from the resulting images. We observed that Aeff and pore angle were strongly related to EOC, texture and depth across the MAP gradient, while tortuosity coefficients related to changes in percent clay and depth. The persistence of row crop agriculture showed considerable strengthening of macropore relationships with soil texture, particularly clay and silt, with aspect ratio/ roundness, and Aeff. The largest takeaway from the findings of this study is that the effect of MAP and the frequency of precipitation events within a given environment influence the number of shrink-swell cycles, particularly in soils with high shrink-swell mineralogy, which impacts linear extensibility and, thus, effective pore area resulting in a lower prevalence of pore spaces capable of transmitting water throughout the soil profile.

References

Ahuja, L. R., Naney, J. W., & Nielsen, D. R. (1984). Scaling Soil Water Properties and Infiltration Modeling 1. *Soil Science Society of America Journal*, *48*(5), 970-973.

Albertson FW (1937) Ecology of mixed prairie in West Central Kansas. *Ecological Monographs* 7:481-547.

Allaire, S. E., Roulier, S., & Cessna, A. J. (2009). Quantifying preferential flow in soils: A review of different techniques. *Journal of Hydrology*, *378*(1-2), 179-204.

Alvarez, C. R., Taboada, M. A., Perelman, S., & Morrás, H. J. M. (2014). Topsoil structure in no-tilled soils in the Rolling Pampa, Argentina. *Soil Research*, *52*(6), 533-542.

Amer, A. M. M., Logsdon, S. D., & Davis, D. (2009). Prediction of hydraulic conductivity as related to pore size distribution in unsaturated soils. *Soil science*, *174*(9), 508-515.

Assouline, S., Tessier, D., & Bruand, A. (1998). A conceptual model of the soil water retention curve. *Water Resources Research*, *34*(2), 223-231.

Banwart, S., Bernasconi, S. M., Bloem, J., Blum, W., Brandao, M., Brantley, S., Chabaux, F., Duffy, C., Kram, P., Lair, G., Lundin, L., Nikolaidis, N., Novak, M., Panagos, P., Ragnarsdottir, K. V., Reynolds, B., Rousseva, S., Ruiter, P., Van Gaans, P., Van Riemsdijk, W., White, T., & Zhang, B. (2011). Soil processes and functions in critical zone observatories: hypotheses and experimental design. *Vadose Zone Journal*, *10*(3), 974-987.

Bark, L. D. (1987). Konza Prairie Research Natural Area, Kansas - the climate of the long-term ecological research sites. *Institute for Arctic and Alpine Research*. Occasional Paper No. 44, pp. 45-50. University of Colorado, Boulder, CO.

Beven, K., & Germann, P. (1982). Macropores and water flow in soils. *Water resources research*, *18*(5), 1311-1325.

Blagodatskaya, E., & Kuzyakov, Y. (2008). Mechanisms of real and apparent priming effects and their dependence on soil microbial biomass and community structure: critical review. *Biology and Fertility of Soils*, *45*(2), 115-131.

Bosse, U., & Frenzel, P. (1997). Activity and distribution of methane-oxidizing bacteria in flooded rice soil microcosms and in rice plants (Oryza sativa). *Applied and Environmental Microbiology*, *63*(4), 1199-1207.

Bouma, J. (1989). Using soil survey data for quantitative land evaluation. In *Advances in soil science* (pp. 177-213). Springer, New York, NY.

Bronick, C. J., & Lal, R. (2005). Soil structure and management: a review. *Geoderma*, *124*(1-2), 3-22.

Brooks, R., & Corey, T. (1964). Hydraulic properties of porous media. *Hydrology Papers, Colorado State University*, *24*, 37.

Carman, P. C. (1937). Fluid flow through granular beds. *Trans. Inst. Chem. Eng.*, *15*, 150-166.

Climatology, S. (1987). Konza prairie research natural area, Kansas. *The Climates of ecological*, 45.

Domenico, P. A., & Schwartz, F. W. 1990, Physical and chemical hydrogeology.

Drager, K. I., Hirmas, D. R., Hasiotis, S. T., & Bents, T. C. (2016). Effects of ant (Formica subsericea) nest development on physical and hydrological properties in a coarse-textured soil. *Soil Science*, *181*(3/4), 166-174.

Eck, D. V., Hirmas, D. R., & Giménez, D. (2013). Quantifying soil structure from field excavation walls using multistripe laser triangulation scanning. *Soil Science Society of America Journal*, *77*(4), 1319-1328.

Eck, D. V., Qin, M., Hirmas, D. R., Giménez, D., & Brunsell, N. A. (2016). Relating quantitative soil structure metrics to saturated hydraulic conductivity. *Vadose Zone Journal*, *15*(1).

Fetter, C. W. (1993). Contaminant hydrogeology macmillan publishing company. *New York, USA*.

Fontaine, S., Bardoux, G., Abbadie, L., Mariotti, A., (2004). Carbon input to soil may decrease soil organic carbon content. *Ecology Letters*, 7, 314–320.

Franzluebbers, A. J. (2002). Water infiltration and soil structure related to organic matter and its stratification with depth. *Soil and Tillage Research*, *66*(2), 197-205.

Gunal, H., & Ransom, M. D. (2006). Clay illuviation and calcium carbonate accumulation along a precipitation gradient in Kansas. *Catena*, *68*(1), 59-69.

Hardie, M., Lisson, S., Doyle, R., & Cotching, W. (2013). Determining the frequency, depth and velocity of preferential flow by high frequency soil moisture monitoring. *Journal of contaminant hydrology*, *144*(1), 66-77.

Hartley, P. E. (2010). *Genesis, mineralogy, and micromorphology of vertic soils in southeastern Kansas* (Doctoral dissertation, Kansas State University).

Heitkamp, F., Wendland, M., Offenberger, K., Gerold, G., (2012). Implications of input estimation, residue quality and carbon saturation on the predictive power of the Rothamsted Carbon Model. *Geoderma,* 170, 168–175.

Hirmas, D. R. (2013). A simple method for removing artifacts from moist fine-textured soil faces. *Soil Science Society of America Journal*, *77*(2), 591-593.

Hirmas, D. R., Giménez, D., Subroy, V., & Platt, B. F. (2013). Fractal distribution of mass from the millimeter-to decimeter-scale in two soils under native and restored tallgrass prairie. *Geoderma*, *207*, 121-130.

Hirmas D. R., Giménez D, Nemes A, Brunsell N. A., and Wilson C. J. 2018. Climate-induced changes in continental-scale macroporosity may intensify the water cycle. Nature.

Jarvis, N. J. (2007). A review of non-equilibrium water flow and solute transport in soil macropores: principles, controlling factors and consequences for water quality. European. *Journal of Soil Science*. 58, 523-162 546.

Jenny, H. (1941). Factors of soil formation. *McGraw-Hill, New York*.

KGS, 1926. Web Address. Data Accessed: June 26, 2020 http://www.kgs.ku.edu/Publications/Bulletins/11/02_ellis.html.

Kozeny, J. (1927). Uber kapillare leitung der wasser in boden. *Royal Academy of Science, Vienna, Proc. Class I*, *136*, 271-306.

Kuzyakov, Y. (2010). Priming effects: interactions between living and dead organic matter. *Soil Biology and Biochemistry*, *42*(9), 1363-1371.

Li, G., Li, X. S., & Li, C. (2017). Measurement of permeability and verification of Kozeny-Carman equation using statistic method. *Energy Procedia*, *142*, 4104-4109.

Li, N., You, M. Y., Zhang, B., Han, X. Z., Panakoulia, S. K., Yuan, Y. R., Liu, K., Qiao, Y.-F., Zou, W.-X., Nikolaidis, N.P. & Banwart, S. A. (2017). Modeling soil aggregation at the early pedogenesis stage from the parent material of a Mollisol under different agricultural practices. In *Advances in Agronomy* (Vol. 142, pp. 181-214). Academic Press.

Luxmoore, R. J., Jardine, P. M., Wilson, G. V., Jones, J. R., & Zelazny, L. W. (1990). Physical and chemical controls of preferred path flow through a forested hillslope. *Geoderma*, *46*(1-3), 139-154.

McBride, M. B. (1989). Surface chemistry of soil minerals. *Minerals in soil environments*, (mineralsinsoile), 35-88.

McCuen, R. H. (1989). *Hydrologic analysis and design* (pp. 143-147). Englewood Cliffs, NJ: Prentice-Hall.

McKenzie, N., & Jacquier, D. (1997). Improving the field estimation of saturated hydraulic conductivity in soil survey. *Soil Research*, *35*(4), 803-827.

Mohammed, A. K., Hirmas, D. R., Nemes, A., & Giménez, D. (2020). Exogenous and endogenous controls on the development of soil structure. *Geoderma*, *357*, 113945.

Mualem, Y. (1986). Hydraulic conductivity of unsaturated soils: prediction and formulas. *Methods of Soil Analysis: Part 1—Physical and Mineralogical Methods*, (methodsofsoilan1), 799-823.

Nissen, T. M., & Wander, M. M. (2003). Management and soil-quality effects on fertilizer-use efficiency and leaching. *Soil Science Society of America Journal*, *67*(5), 1524-1532.

Norris, M. D., Blair, J. M., & Johnson, L. C. (2001). Land cover change in eastern Kansas: litter dynamics of closed-canopy eastern redcedar forests in tallgrass prairie. *Canadian Journal of Botany*, *79*(2), 214-222.

NRCS. (2005). Soil Properties and Qualities. 430-VI-NSSH Section 618, Page 25).

Oades, J. M. (1989). An introduction to organic matter in mineral soils. *Minerals in soil environments*, (mineralsinsoile), 89-159.

Price, K., Jackson, C. R., & Parker, A. J. (2010). Variation of surficial soil hydraulic properties across land uses in the southern Blue Ridge Mountains, North Carolina, USA. *Journal of hydrology*, *383*(3-4), 256-268.

Rawls, W. J., Gimenez, D., & Grossman, R. (1998). Use of soil texture, bulk density, and slope of the water retention curve to predict saturated hydraulic conductivity. *Transactions of the ASAE*, *41*(4), 983.

Robinson, D. A., Jones, S. B., Lebron, I., Reinsch, S., Domínguez, M. T., Smith, A. R., Jones, D. L., Marshall, M. R., & Emmett, B. A. (2016). Experimental evidence for drought induced alternative stable states of soil moisture. *Scientific reports*, *6*(1), 1-6.

Robinson, D. A., Hopmans, J. W., Filipovic, V., van der Ploeg, M., Lebron, I., Jones, S. B.,

Reinsch, S., Jarvis, N., & Tuller, M. (2019). Global environmental changes impact soil hydraulic functions through biophysical feedbacks. *Global change biology*, *25*(6), 1895-1904.

Schaap, M. G., Leij, F. J., & Van Genuchten, M. T. (2001). Rosetta: A computer program for estimating soil hydraulic parameters with hierarchical pedotransfer functions. *Journal of hydrology*, *251*(3-4), 163-176.

Schafer, W. M., & Singer, M. J. (1976). A New Method of Measuring Shrink-Swell Potential Using Soil Pastes 1. *Soil Science Society of America Journal*, *40*(5), 805-806.

Schoewe, W. H. (1949). The geography of Kansas: Part II. Physical geography. *Transactions of the Kansas Academy of Science (1903-)*, *52*(3), 261-333.

Seneviratne, S. I., Corti, T., Davin, E. L., Hirschi, M., Jaeger, E. B., Lehner, I., Orlowsky, B., & Teuling, A. J. (2010). Investigating soil moisture–climate interactions in a changing climate: A review. *Earth-Science Reviews*, *99*(3-4), 125-161.

Šimunek, J., Šejna, M., & Van Genuchten, M. T. (1998). The HYDRUS-1D software package for simulating the one-dimensional movement of water, heat, and multiple solutes in variably-saturated media, Version 2.0, 202 pp. *Rep. IGWMC-TPS*, *70*.

Smith, R. E., Smettem, K. R., & Broadbridge, P. (2002). *Infiltration theory for hydrologic applications*. American Geophysical Union.

Soil Survey Staff, 2014. Kellogg Soil Survey Laboratory Methods Manual. Soil Survey Investigations Report No. 42, Version 5.0. Burt, R., Soil Survey Staff (Eds.). U.S. Department of Agriculture, Natural Resources Conservation Service.

Steffens, M., Kohlpaintner, M., & Buddenbaum, H. (2014). Fine spatial resolution mapping of soil organic matter quality in a Histosol profile. *European journal of soil science*, *65*(6), 827-839.

Stewart, R. D., Abou Najm, M. R., Rupp, D. E., Lane, J. W., Uribe, H. C., Arumí, J. L., &

Selker, J. S. (2015). Hillslope run-off thresholds with shrink–swell clay soils. *Hydrological Processes*, *29*(4), 557-571.

Thevenot, M., Dignac, M. F., & Rumpel, C. (2010). Fate of lignins in soils: a review. *Soil Biology and Biochemistry*, *42*(8), 1200-1211.

Van Looy, K., Bouma, J., Herbst, M., Koestel, J., Minasny, B., Mishra, U., Montzka, C., Nemes, A., Pachepsky, Y., Padarian, J., Schaap, M., Tóth, B., Verhoef, A., Vanderborght, J., van der Ploeg, M.J., Weihermüller, L., Zacharias, S., Zhang, Y., & Vereecken, H. (2017). Pedotransfer functions in Earth system science: Challenges and perspectives. *Reviews of Geophysics*, *55*(4), 1199-1256.

Watson, K. W. & Luxmoore, R. J. Estimating macroporosity in a forest watershed by use of a166 tension infiltrometer. Soil Sci. Soc. Am. J. 50, 578–582 (1986).

Wehmueller, W. A. (1996). *Genesis and morphology of soils on the Konza Prairie Research Natural Area, Riley and Geary Counties, Kansas* (Master's thesis, Kansas State University).

Welch, J. E., & Hale, J. M. (1987). Pleistocene loess in Kansas—Status, present problems, and future considerations. *Quaternary environments of Kansas: Kansas Geological Survey Guidebook Series*, *5*, 67-84.

Wiesmeier, M., Poeplau, C., Sierra, C.A., Maier, H., Frühauf, C., Hübner, R., Kühnel, A., Spörlein, P., Geuß, U., Hangen, E., Schilling, B., von Lützow, M., Kögel-Knabner, I., (2016).

Projected loss of soil organic carbon in temperate agricultural soils in the 21st century: effects of climate change and carbon input trends. *Scientific Reports* , 6, 32525.

Wösten, J. H. M., Pachepsky, Y. A., & Rawls, W. J. (2001). Pedotransfer functions: bridging the gap between available basic soil data and missing soil hydraulic characteristics. *Journal of hydrology*, *251*(3-4), 123-150.

7 Appendices

7.1 Appendix A: *Soil Excavation Procedure*

Introduction

The tray method is the excavation of soil on the pedon scale through the use of steel trays, as shown in Figure 1.0. Three sites (Welda, Konza, and Hays) and three land uses (Prairie, Restored Prairie, Agricultural) will be used for the soil excavation. Once the soil is collected, root density, macropore distribution, and chemical variation of the soil will be visualized by using multistripe laser triangulation (MLT) and hyperspectral scanning techniques.

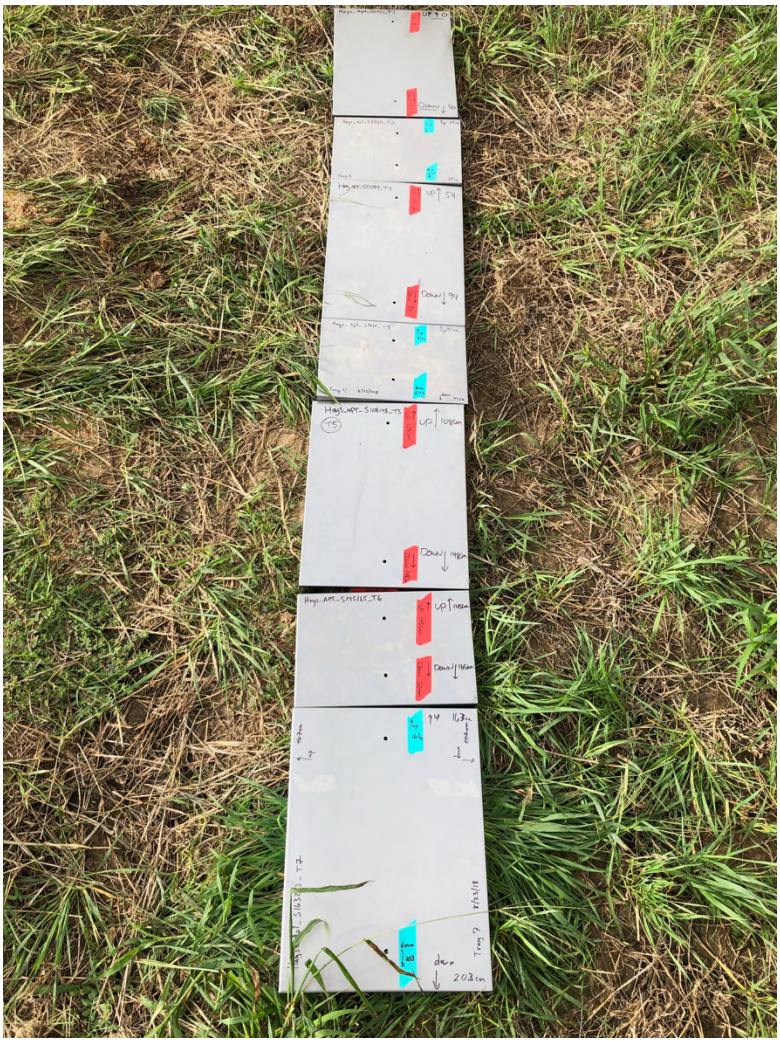

Figure 1.0 - Steel soil trays stacked on top of each other. This is an example of how a soil pit is excavated.

Site Description

Welda -- this site is located in Eastern Kansas near Ottawa, KS and ~60 mi south of the University of Kansas, Lawrence. Welda is within the Osage Cuestas, which are a series of escarpments made of alternating layers of Pennsylvanian-age limestone and shale with a short, sharp slope on one side, and a long gentle slope on the other. Over time, differential erosion occurs as a result of the limestone and shale weathering unevenly; thus producing the cuesta (Schoewe, 1949).

Konza -- this site is formally known as the Konza Prairie Natural Research Area (KPNRA); which is located ~10km south of Manhattan, KS and Kansas State University. The KPNRA is located within the Flint Hills, which are upland escarpments similar to the eastern Osage Cuestas within a temperate midcontinental climate (Bark, 1987). The Flint Hills express a unique terraced, or "benched" shape facing the east-west directions along with a limestone cap containing a significant amount of flint, which makes it more resistant to weathering (Schoewe, 1949).

Konza Prairie, Kansas

Hays -- this site is located near the Agricultural Research Station just south of Hays and Fort Hays State University off US Highway 183. Located in Western Kansas within the High Plains region, it is the driest of the three sites selected (580mm; 75% in fall and spring) with a mean annual temperature of 12 degrees C (Lauenroth & Radler, 2008). This site is flat with tall grasses and shrubs present, but very few trees; resulting in little canopy cover and thus direct sunlight exposure. The soils express thick, dark A-horizons with carbonate accumulation in the subsurface, which was shown by the five consecutive Btk horizons in the natural prairie and agricultural sites.

Hays, Kansas

Table 1.0 - comparison of region, elevation, and mean annual precipitation of the three study sites.

	Welda	Konza	Hays
Geomorphic Region	Osage Cuestas	Flint Hills	High Plains
Elevation (m)	335	330	616
Mean Annual Precipitation (mm)	1,012	835	580

Materials

- 5X Soil knives
- 3X Sharpened trowels
- 100 Steel trays at 30 x 20 x 4 cm and 50 at 30 x 40 x 4 cm
- 2X Rock hammers
- 2x Spades and 2x Sharpshooters
- Wrapping material
- 3x Rolls of labeling tape
- Sharpies
- Ziploc bags
- 2x Clippers
- 1x Coolers
- Steel chisels
- Pop-up tents
- Scissors

Soil Excavation Procedure

1. Clean off and level a soil pit face using a sharpened trowel or knife.
2. Measure the depth of the soil pit and note the depths of all horizon boundaries. This is important to know how many trays to use and where to place them. **There will be a 2.5 cm burn zone for each MLT scan so it is essential to have at least a 5 cm overlap for each soil tray to prevent gaps in the final image.**
3. Take note of coarse fragment locations and plan to place the trays away from these areas if possible.
4. Take pictures and notes of the soil pit and the surrounding landscape prior to excavation.
5. Label relevant information (see labeling scheme section) on the tray such as depth, direction, and location.
6. Place the steel tray on the surface of the soil and make an outline of the area using a knife **Be sure to never step on the soil surface where you are extracting.**
7. Sequentially pick away at the perimeter of the tray until the desired area is raised enough to take the sample.
8. Using a rock hammer, hit the tray into the soil face so that it fills to the bottom (there should be holes on the back of the tray to help see when it is full).
9. Insert field knives or nails on the bottom of the tray to stabilize it.
10. Continue to hammer field knives up the sides, then over the top of the tray to start separating it from the soil face.

11. When the entire perimeter of the tray is detached from the soil face, gently pull the two knives at the top of the tray downward and toward you. **Make sure someone is prepared to catch and hold the tray when it is completely removed from the soil face.**
12. Clean the soil off the top of the tray and wrap the surface. Be sure to take one soil sample for each tray and place into a labeled Ziploc bag for gravimetric moisture analysis.
13. Preserve the soil the best as possible by placing it in a cooled, shaded area, keeping the tray out of the sun and in the shade, wrapped and stored as not to be damaged during transport, and placed on ice as soon as possible.

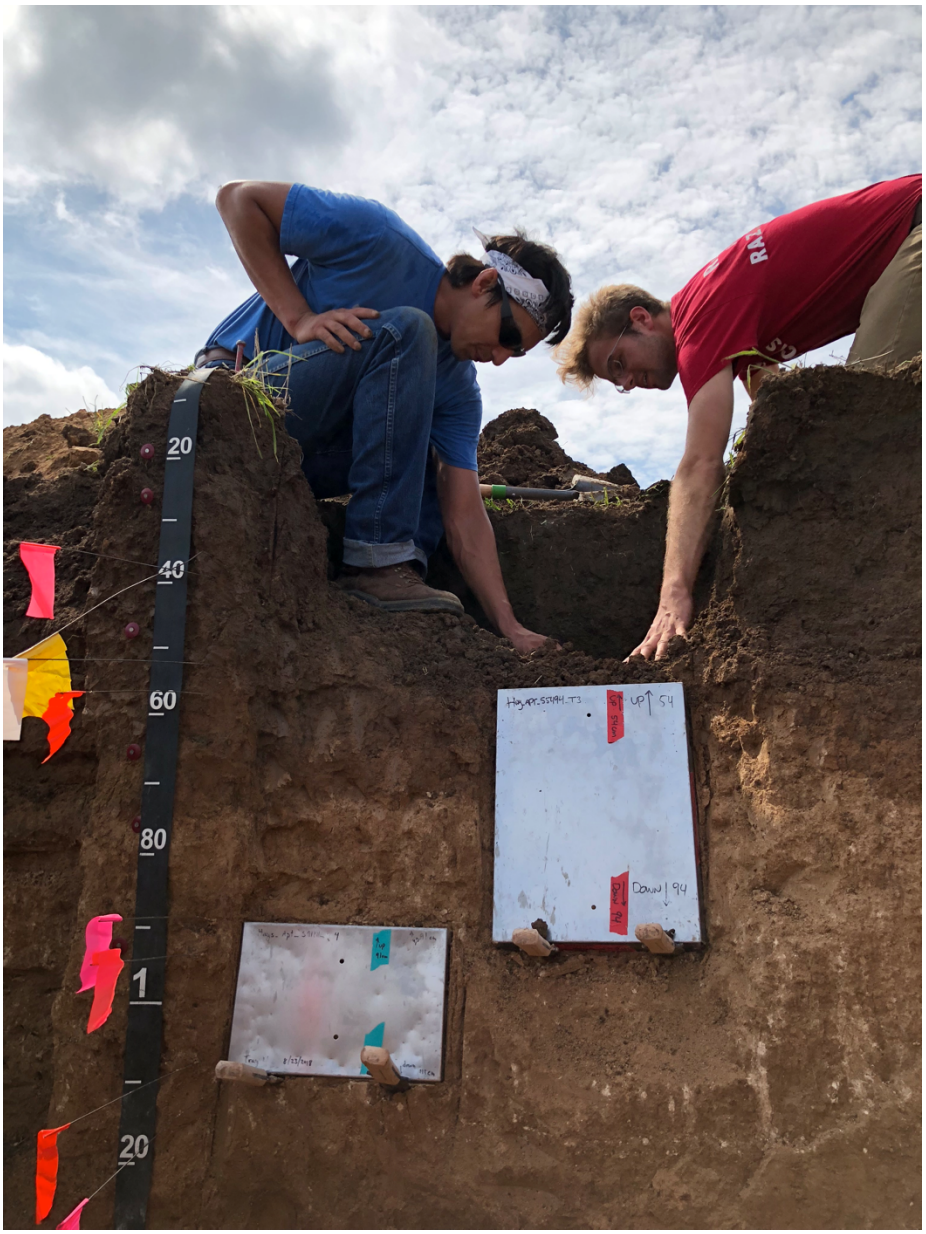

Figure 2.0 - Example of how the steel trays were placed into the soil for excavation. Note how the knives below are supporting the tray -- the entire perimeter of the tray was carved and chiseled before removal.

Labeling Scheme (Trays and Ziploc Bags for Gravimetric Moisture)

Write the name of the site (Welda, Konza, Hays) as well as the land use for the site Native Prairie (Npt), Post-Ag Prairie (Ppt), and Agriculture (Apt) on each tray to distinguish which location the sample was taken.

Write the depth at which the tray was excavated (e.g. 0 - 20 cm (S020) and 20 - 40 (S2040) for the 20 cm trays and 0 - 40 cm (S040), 40 - 80 cm (S4080), for the 40 cm trays, ect.).

Also be sure to determine which side was facing up, and which side was facing down. To do this, draw an arrow and write "up" or "down" on the correct side.

For tray number, write the order in which the sample was taken. For example, the first tray would be "T1", the second would be "T2", ect.

Finally, write initials, date, and any other relevant information on the tray.

For example, a Hays soil pit in an agricultural field that was excavated with a 40 cm tray from the surface would be labeled as "Hays_Apt_S040_T1". To account for a burn zone, an overlap should be given for each tray. If using a 20 cm tray, the next label would look something like "Hays_Apt_S3757_T2".

*** Be sure to label all relevant information prior to excavation! ***

Transport Back to the Lab

1. About 6 - 7 trays will be used for every 2 meters of soil analyzed. If the trays need to be stacked, it is important that they do not crush each other. To avoid this, it may be helpful to stack moving pallets and place the soil trays in between the boards when transporting.
2. When returning to the lab, make sure that a cold storage room is ready (an inspection of the room should be made prior to excavation to know how the soil trays will be stored).

7.2 Appendix B: Sensor Installation

Introduction

Dataloggers are used to effectively record measured parameters such as CO2, O2, soil moisture (VWC), temperature, and matric potential in the environment. Multiplexers are used when a lot of sensors (and thus ports), are required to take these measurements.

Required Materials (Per Site)

- 1x CR1000X datalogger
- 2x AM 16/32B multiplexers
- 1x 12V battery
- 1x CH150 battery regulator
- 3x Apogee SO-120 oxygen sensors
- 3x EOS CO2 sensors
- 3x 5TM soil moisture sensors
- 1x Soil matric potential sensor
- 1x RV50 communication device
- 2x Iron rods
- Metal cloth
- 3x Terminal blocks
- 1x Computer that can connect through USB
- 1x Solar panel
- 2x U-Bolts
- Zip-ties
- 1x Soil auger
- Cement
- 2x Metal ties
- Trowels/ shovels
- 3x Putty packs
- 1x Desiccant pack
- 20-gauge copper bell wire

Coding

Coding is performed in the LoggerNet CRBasic Editor. It is important to note that the CO2 and O2 sensors are set to take one measurement every hour, while the soil moisture and matric potential sensors are set to take one measurement every 30 minutes.

The Konza Series was coded from Soil_Lab.CR1X. Each DataLogger has a different name and a slightly different variation of Konza_I_Code.CR1X in order to calibrate the multiplier (CF) and offset (OFFST) for each O2 sensor as shown below.

If a CO2 sensor is not showing reasonable measurements, an additional code (EosGP.CR1X) can be used to directly connect the sensor and take a measurement.

Konza_II	Konza_II_Code.CR1X
Konza_III	Konza_III_Code.CR1X
Welda_I	Welda_I_Code.CR1X
Welda_II	Welda_II_Code.CR1X
Welda_III	Welda_III_Code.CR1X
Hays_I	Hays_I_Code.CR1X
Hays_II	Hays_II_Code.CR1X
Hays_III	Hays_III_Code.CR1X

Power Source

The datalogger and multiplexers are connected to a 12V battery power supply that is going to be recharged by solar panels in the field. In order to power all of the sensors in the setup, (3x) terminal blocks are going to be used. These terminal blocks will "bundle" wires from like-sensors together in order to complete a connection. Please note that the CO2 sensors are connected to the 12V (and will not use the terminal blocks, rather all red wires will be placed in the 12V terminal of the datalogger) and the O2 sensors are connected to the SW12-1 ports in this manner. There should be one 20-gauge copper bell wire connecting the terminal block to each respective port (see wiring diagram below).

Wiring

There is one datalogger and two multiplexers (MUXs) for each sensor setup. The first multiplexer, (MUX_1), has the (3x) CO2 and (3x) O2 sensors connected; and thus takes one measurement every hour. The second multiplexer (MUX_2) has the (3x) soil moisture and (1x) matric potential sensors connected to it and takes one measurement every 30 minutes.

Company: University of Kansas
Project: SO #332722
Documented By: Bart Nef - CSI
Date: 10.Aug.2018

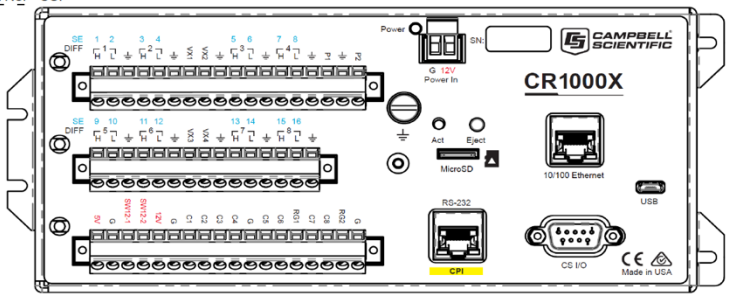

	5V
BLK: RV50; G Terminal Block	G
12V-1 Terminal Block	SW12-1
Mux #2 ODD L	SW12-2
RED: RV50; 12V Terminal Block	12V
G: MUX #1 & MUX #2	G
CLOCK: MUX #1	C1 (COM1 Tx)
RESET: MUX #1	C2 (COM1 Rx)
CLOCK: MUX #2	C3 (COM2 Tx)
RESET: MUX #2	C4 (COM2 Rx)
GND SYMBOL: MUX #2	G
ODD H : MUX #2	C5 (COM3 Tx)
WHITE: RV50	C6 (COM3 Rx)
	RG1
	C7 (COM4 Tx)
	C8 (COM4 Rx)
	RG2
	G

RED: 12V CH150	12V
BLACK: G CH150	G

ODD H: MUX #1	5H (SE9)
ODD L: MUX #1	5L (SE10)
GND SYMBOL: MUX #1	
	6H (SE11)
	6L (SE12)
	VX3
	VX4
	7H (SE13)
	7L (SE14)
	8H (SE15)
	8H (SE15)

	1H (SE1)
	1L (SE2)
	2H (SE3)
	2L (SE4)
	VX1
	VX2
	3H (SE5)
	3L (SE6)
	4H (SE7)
	4L (SE8)
	P1
	P2

SENSOR POWER SPECIFICATIONS

SO-120 Apogeen Oxygen Sensor

Voltage Input	12vdc
Current Usage	Heater: ~ 6.2mA
Warm Up Time	1 minute

eosGP CO2 Sensor

Voltage Input	5 to 24vdc
Current Usage	< 1W (@13vdc current usage = 76mA)
Warm Up Time	< 30 min (!)

Meter ECH2O 5TM VWC Sensor

Voltage Input	3.6 to 15 vdc
Current Usage	3.0 mA Typical; 10mA Maximum
Warm Up Time	Maximum: 200ms

Meter TEROS21 SOIL MATRIX Sensor

Voltage Input	3.6 to 15 vdc
Current Usage	0.03mA quiescent; 10mA maximum
Warm Up Time	200ms

Daily Current Amp-Hrs

Qty	Amp-hrs
3	2.736

MUX #1

Company: University of Kansas
Project: SO #332722
Documented By: Bart Nef - CSI
Date: 08.Aug.2018

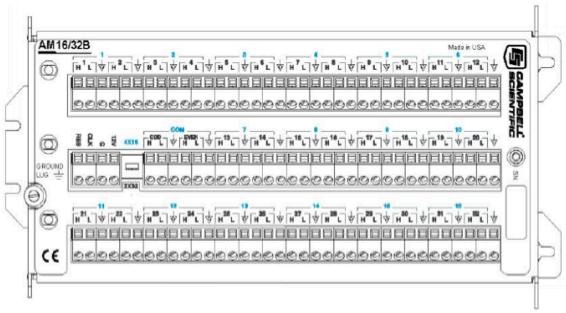

	G
BLACK: C02 #2	6 EL (12L)
GRAY: C02 #2	6 EH (12H)
	G
BLACK: C02 #2	6 OL (11L)
PURPLE: C02 #2	6 OH (11H)
	G
BLACK: C02 #2	5 EL (10L)
BLUE: CO2 #2	5 EH (10H)
	G
BLACK: C02 #1	5 OL (9L)
GRAY: C02 #1	5 OH (9H)
	G
BLACK: C02 #1	4 EL (8L)
PURPLE: C02 #1	4 EH (8H)
	G
BLACK: C02 #1	4 OL (7L)
BLUE: CO2 #1	4 OH (7H)
	G
RED: O2 TC #3	3 EL (6L)
YELLOW: O2 TC #3	3 EH (6H)
	G
BLACK: O2 #3	3 OL (5L)
WHITE: O2 #3	3 OH (5H)
	G
RED: O2 TC #2	2 EL (4L)
YELLOW: O2 TC #2	2 EH (4H)
	G
BLACK: O2 #2	2 OL (3L)
WHITE: O2 #2	2 OH (3H)
	G
RED: O2 TC #1	1 EL (2L)
YELLOW: O2 TC #1	1 EH (2H)
	G
BLACK: O2 #1	1 OL (1L)
WHITE: O2 #1	1 OH (1H)

	G
	10 EL (20L)
	10 EH (20H)
	G
	10 OL (19L)
	10 OH (19H)
	G
	9 EL (18L)
	9 EH (18H)
	G
	9 OL (17L)
	9 OH (17H)
	G
	8 EL (16L)
	8 EH (16H)
	G
BLACK: C02 #3	8 OL (15L)
GRAY: C02 #3	8 OH (15H)
	G
BLACK: C02 #3	7 EL (14L)
PURPLE: C02 #3	7 EH (14H)
	G
BLACK: C02 #3	7 OL (13L)
BLUE: CO2 #3	7 OH (13H)
	G
	EVEN L
	EVEN H
GROUND SYMBOL: CR1000X	G
5L: CR1000X	ODD L
5H: CR1000X	ODD H
	2X32 MODE
12V TERMINAL BLOCK	12V
G: CR1000X	G
C1: CR1000X	CLOCK
C2: CR1000X	RESET

	G
	16 EL (32L)
	16 EH (32H)
	G
	16 OL (31L)
	16 OH (31H)
	G
	15 EL (30L)
	15 EH (30H)
	G
	15 OL (29L)
	15 OH (29H)
	G
	14 EL (28L)
	14 EH (28H)
	G
	14 OL (27L)
	14 OH (27H)
	G
	13 EL (26L)
	13 EH (26H)
	G
	13 OL (25L)
	13 OH (25H)
	G
	12 EL (24L)
	12 EH (24H)
	G
	12 OL (23L)
	12 OH (23H)
	G
	11 EL (22L)
	11 EH (22H)
	G
	11 OL (21L)
	11 OH (21H)

MUX #2

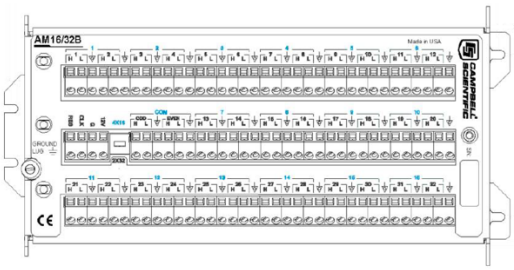

		G			G		G
		6 EL (12L)			10 EL (20L)		16 EL (32L)
		6 EH (12H)			10 EH (20H)		16 EH (32H)
		G			G		G
		6 OL (11L)			10 OL (19L)		16 OL (31L)
		6 OH (11H)			10 OH (19H)		16 OH (31H)
		G			G		G
		5 EL (10L)			9 EL (18L)		15 EL (30L)
		5 EH (10H)			9 EH (18H)		15 EH (30H)
		G			G		G
		5 OL (9L)			9 OL (17L)		15 OL (29L)
		5 OH (9H)			9 OH (17H)		15 OH (29H)
		G			G		G
		4 EL (8L)			8 EL (16L)		14 EL (28L)
		4 EH (8H)			8 EH (16H)		14 EH (28H)
		G			G		G
		4 OL (7L)			8 OL (15L)		14 OL (27L)
		4 OH (7H)			8 OH (15H)		14 OH (27H)
		G			G		G
		3 EL (6L)			7 EL (14L)		13 EL (26L)
		3 EH (6H)			7 EH (14H)		13 EH (26H)
		G			G		G
		3 OL (5L)			7 OL (13L)		13 OL (25L)
		3 OH (5H)			7 OH (13H)		13 OH (25H)
CLEAR: TEROS21		G			G		G
BROWN: TEROS21		2 EL (4L)			EVEN L		12 EL (24L)
ORANGE: TEROS21		2 EH (4H)			EVEN H		12 EH (24H)
CLEAR: 5TM #3		G	G: CR1000X		G		12 OL (23L)
BROWN: 5TM #3		2 OL (3L)	SW12-2: CR1000X		ODD L		12 OH (23H)
ORANGE: 5TM #3		2 OH (3H)	C5: CR1000X		ODD H		G
CLEAR: 5TM #2		G			2X32 MODE		11 EL (22L)
BROWN: 5TM #2		1 EL (2L)		12V	12V		11 EH (22H)
ORANGE: 5TM #2		1 EH (2H)	12V TERMINAL BLOCK	G	G		G
CLEAR: 5TM #1		G	G: CR1000X	CLK	CLOCK		11 OL (21L)
BROWN: 5TM #1		1 OL (1L)	C3: CR1000X	RES	RESET		11 OH (21H)
ORANGE: 5TM #1		1 OH (1H)	C4: CR1000X				

Three terminal blocks for each system will be required.
Terminal block designation reflects the connection to the CR1000X.
More than one wire can go into any terminal block terminal.

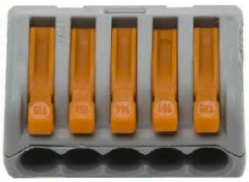

SW12-1 TERMINAL BLOCK WIRE CONNECTIONS
SW12-1 on the CR1000X.
All yellow wires from all SO-120 O2 sensors cable #1 (not the yellow thermocouple wire)
All red wires from the eosGP CO2 power cable.

G TERMINAL BLOCK WIRE CONNECTIONS
G (any G) on the CR1000X
All blue and clear (shield) wires from the SO120 O2 sensors.
All black wires from the eosGP CO2 sensor power cables.
All clear (shield) wires from the eosGP CO2 sensors

12V TERMINAL BLOCK CONNECTIONS
12V on the CR1000X
Mux #1 and Mux #2 12V

Sensor Wire Colors for Sullivan Installation

SO-120 Apogeen Oxygen Sensor (Qty 3)

Cable #1 O2 Sensor

Wire Color	Description
Yellow	12V
White	O2 Diff H
Black	O2 Diff L
Blue	Ground
Shield/Clear	Ground
Cable #2 Type K Thermocouple	
Wire Color	Description
Yellow	Diff H
Red	Diff L

eosGP CO2 Sensor (Qty 3)

Wire Color	Description
Red (Pwr Cbl)	12V
Purple	Low CO2 Diff H
Black (Gnd Cable)	Low CO2 Diff L
Gray	High CO2 Diff H
Black (Gnd Cable)	High CO2 Diff L
Blue	Temp Diff H
Black (Gnd Cable)	Temp Diff L
Black (Pwr Cbl)	Ground
Shield/Clear	Ground

Meter ECH2O 5TM VWC Sensor (Qty 3)

Wire Color	Description
Brown	12V
Orange	SDI12
Bare	Ground

Meter TEROS21 SOIL MATRIX Sensor (Qty 1)

Wire Color	Description
Brown	12V
Orange	SDI12
Bare	Ground

CH150 WIRING

PS150 Terminal	Connection
G (next to Solar)	Black: Solar Panel
Solar	Red: Solar Panel
G (next to 12V)	Black: G CR1000X Power Terminal Block
12V	Red: 12V CR1000X Power Terminal Block
Battery Connector	Battery Cable from BP12

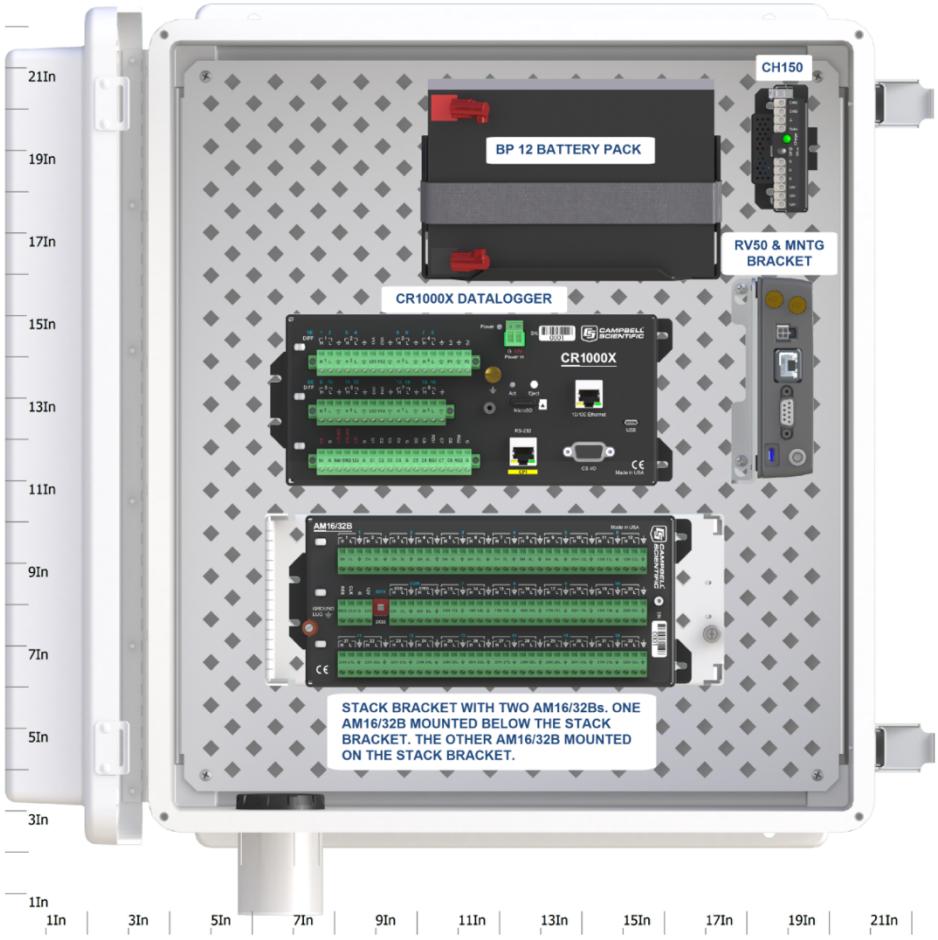

Field Preparation

There are many important things to do before deploying in the field to make sure that the sensors are working properly and are ready to go:

1. Pre-assemble the weather box to look like the figure above. Do not have any wires connected during transport. Please note that there are three PVC "outlets" on the bottom of each weather box, divide the wiring for each sensor through each outlet (for example, CO2 wiring would go through one, O2 wiring through another, and 5TM soil moisture and matric potential sensor wiring through the third. This is where the color-coding and labeling can be useful).
2. Develop a labeling and color-coding scheme for the sensors according to your personal organization. It is important to effectively label the sensors/ wires with tape in order to identify them once they are place in the ground.
3. **Check the sensors.** Make sure that everything is working properly before going into the field, not just the sensors but also the wiring and coding. Place the soil moisture and

matric potential sensors into potting mix or soil in the lab and record the response. Perform an ambient air check on the CO2 and O2 sensors.
4. Record the manufacturing ID information of each sensor in a notebook or word processing program.
5. Pack and organize the equipment, preferably by site before going into the field.

Field Installation

There are a lot of parts involved to get a sensor setup working in the field. Here is a comprehensive step-by-step approach to get the job done effectively:

6. Place an iron rod 2 meters into the soil using a soil auger and cement into the ground.
7. Attach the weather box onto the iron rod by using a metal tie.
8. Secure the solar panel with a U-bolt that will recharge the 12V battery.
9. Start placing the sensors into the ground at 10, 40, and 120 cm (130 cm for matric potential sensor) by digging a hole around the sensor and filling around it.
10. Dig a small trench from the top of the soil pit to the weather box, where all of the wires will be wrapped in metal cloth and zip-tied in an organized fashion.
11. Feed all wires through a second metal pipe and connect it to the bottom of a PVC outlet at the bottom of the weather box.
12. Wire all sensors to the datalogger and multiplexers.
13. Perform field system checks on the software (both manual and autonomous) to make sure the sensors are responding accordingly.
14. Seal all PVC outlets with putty, wrap any exposed wires with metal cloth by zip-tie, and make sure a desiccant pack is in the weather box before leaving the site.

Scheduled Monitoring

It is important to return to your site regularly (every 2 - 4 weeks) to collect data and to make sure that everything is working properly.

- Collect the data from a computer that can connect to the datalogger through USB.
- Make sure wires do not become exposed in any way.
- Replace the desiccant pack on each trip.

Troubleshooting

Issues with data collection are likely to occur. Here are some things to look for and potential ways to solve them:

- **NAN Values -** this likely means that a multiplexer(s) is not properly wired to the datalogger. Be sure to check that all wires are secured. If the wiring is not the issue, look to the written program and make sure the timing of each sensor is in sync with the datalogger.

- **Negative Values -** in this case, the multiplexer is probably connected properly but a sensor is not. Look to make sure the wiring from the sensors is secure.
- **Values Out of Range -** this may be an issue with the sensor itself. Be sure to contact the manufacturer to know how the sensor was calibrated, if there is something you can do to fix it, or if it needs to be returned to be re-calibrated.

7.3 Appendix C: MLT Scanning Procedure

Introduction

Soil structure is often qualitatively described in the field through profile descriptions, but in recent decades high-resolution laser scanning has been employed to quantitatively describe soil pores larger than 125 μm in diameter. In order to achieve a better understanding of soil macroporosity, a multistripe laser triangulation (MLT) technique can be used. This technique involves the release one or more laser stripes to form a 3D image of the soil surface, and is an effective way to digitize and record soil structure and porosity. Aggregates can be effectively digitized to a volume of 1 cm^3 using this method. Coupling MLT scanning with high-resolution sensing techniques can enhance the detection of macropore and soil structure spatial arrangement (Hirmas et al., 2013).

Materials (Including Shelf)

2x Wood Planks (2"x 4" x 2')

1x Wood Plank (2" x 2" x 4')

2x Wood Screws (dim)

5x Tapcon cement screws (dim)

Wooden Platform for MLT Scanner (dim)

Bolts

Nuts

Washers

Level

Power Drill

Tapcon Cement Drill Bit (dim)

Wood Drill bit(s) (dim)

2x L-Braces

MLT Scanner + Power Source

Computer with USB connection

Soil Trays

Tape measure(s)

Shelf Installation

It is important to place the MLT scanner on a level surface that is 6.5" above the soil tray being scanned (but having the scanner slightly higher will be better for flexibility). In order to accomplish this, a shelf can be mounted on the side of a wall to support the scanner. An installation procedure is described below using the materials listed above:

1. Make sure the shelf is in a position where the scanner will have access to a power source and a computer with USB connection.
2. Mark off a 4' section of wall space to mount the 2"x 2" wood plank and the points where the Tapcon cement (or whatever material) screws are being drilled in (3x were used here).
3. Drill three screws through the 2" x 2" wood plank and into the wall (this step may require two people -- one to drill and another to hold the other end of the 2" x 2" wood plank).
4. Bolt the 2x L-braces onto the (2x) 2" x 4" wood planks (this will also go through the scanning platform -- it will be easiest if everything is pre-drilled) to create a manifold.
5. Using wood screws, drill through the (2x) 2" x 4" wood planks that are part of the manifold into the 2" x 2" that is attached to the wall.
6. Drill two more Tapcon cement screws into the top of the 2x L-braces (a 1-2" spacer may be required to account for the width of the 2" x 2" wood plank in the wall).
7. Check to make sure the manifold is level on all sides and has the structural stability to support the scanner.

Soil Preparation

The process of soil collection will likely leave a smeared and uneven surface on the sample. This section explains how to properly prepare the sample before scanning.

1. Take a soil tray from cold storage and open it. Take a picture of the sample before any preparation.
2. Level the soil to ~0.5 cm above the tray surface.
3. Lay the soil out to dry in order to fully express macropores. This process may take 1 - 3 days and depends on the sample itself. **Note -- there is an optimal soil moisture range. Check all soils after 24 hours to makes sure they are not too dry.**
4. Using tap or DI water, spray down the surface of the soil tray.

5. Invert a can of compressed air and spray the moistened area. This should create a frozen layer on the surface of the soil.
6. Using dental tools, pick just below the frozen layer (~ 0.5 cm deep) to expose the soil underneath. Be sure to minimize pick marks or smears after this point.
7. Clip any roots to the level soil surface.
8. Make sure the final product is as even and level as possible -- this is important for the quality of the resulting scans. **If the soil is still uneven, work from the high points, not from the low points. It is ideal to keep the soil at/ slightly higher than the height of the tray.**
9. When finished with preparation, take another picture of the sample for records.

Figure 2.0 - Example of the soil freezing method.

Gravimetric Moisture Content Procedure

Collect soil from each horizon for gravimetric moisture analysis. It is important to determine how much moisture is present in the soil at each depth during the time of scanning, so this process must be performed simultaneously with the MLT procedure. This section will give a brief overview of how gravimetric moisture in soils is determined.

1. Label three crinkle tins for each horizon collected. For example, if a Konza soil used for row-crop agriculture is collected and the Ap horizon is from 0-39 cm, the samples could be labeled Ap039-KNZA-1, 2,3..
2. Be sure to weigh and record the weight of each tin, then "TAR" the scale.
3. Place 1.0 g (+/- 0.01 g) of soil into each tin. Record the weight.
4. Place the tins into an autoclave for 24 hours at 105 degrees C.
5. Record the weight of the soil + tin when taken out of the autoclave.
6. Use the equation (Wet - Dry)/ (Dry) to determine the gravimetric moisture of the soil (it should be in a percent).

MLT Scanning Procedure

1. Connect the scanner to the computer through USB.
2. Connect to the ScanStudio software by NextEngine. **Make sure no other programs are running at this time!**
3. Place the soil tray 6.5" below the scanner.
4. On ScanStudio, select "HD" and "Single Scan" set at "Neutral" with range set at "Macro".
5. Mark the depth of the sample by cm using red lettering on yellow tape. You may also identify horizon boundaries. be sure the scanner is marked on each side of the tray so it is visible in each image.
6. The perimeter of each image will have a 2.5 cm burn zone (in other words it will not be used due to edge effect).
7. When scanning the right-hand side of the tray, be sure to position extra far to the right to make sure the image is center.
8. Click "start scan" and make sure there is no light in the room when scanning.
9. Save every time you scan (each tray will be saved as one file, and all "sub-scans" will be contained within that file **Make sure there are no spaces in file names!**
10. Create a folder to place all of the scans.
11. Be sure to regularly back files to an external hard drive.

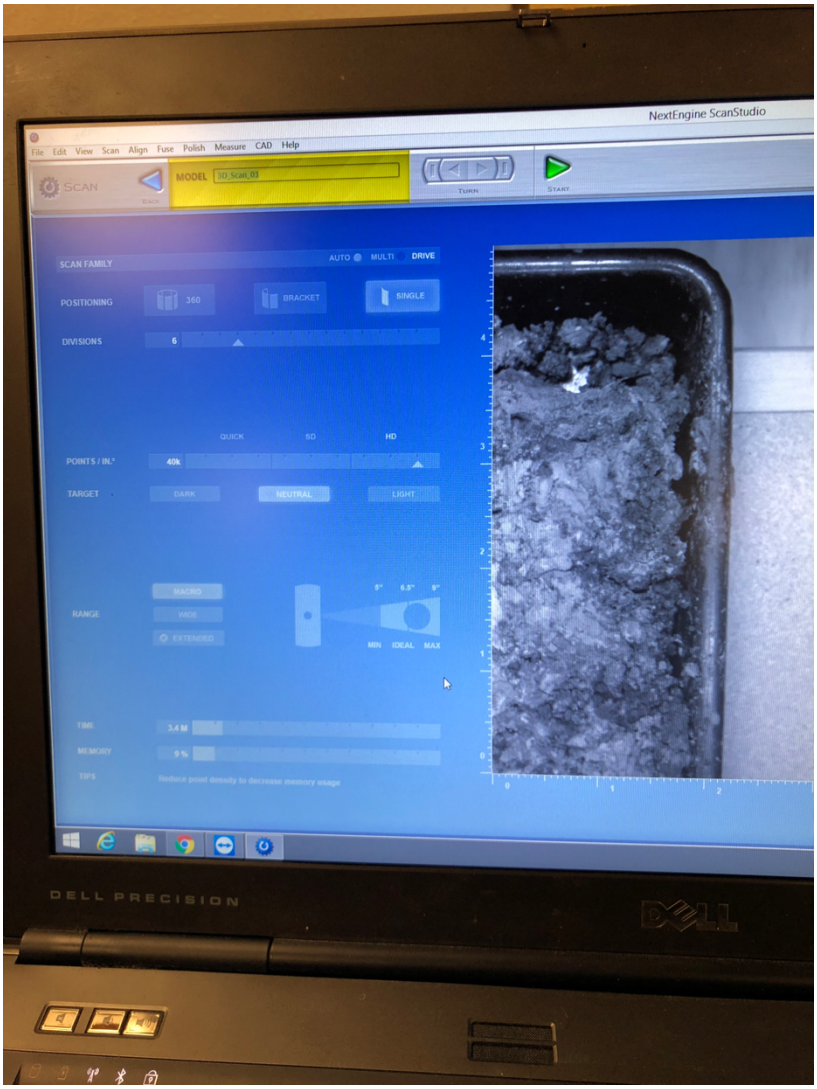

Figure 3.0 - Before taking a scan in ScanStudio, make sure all of the settings are properly selected.

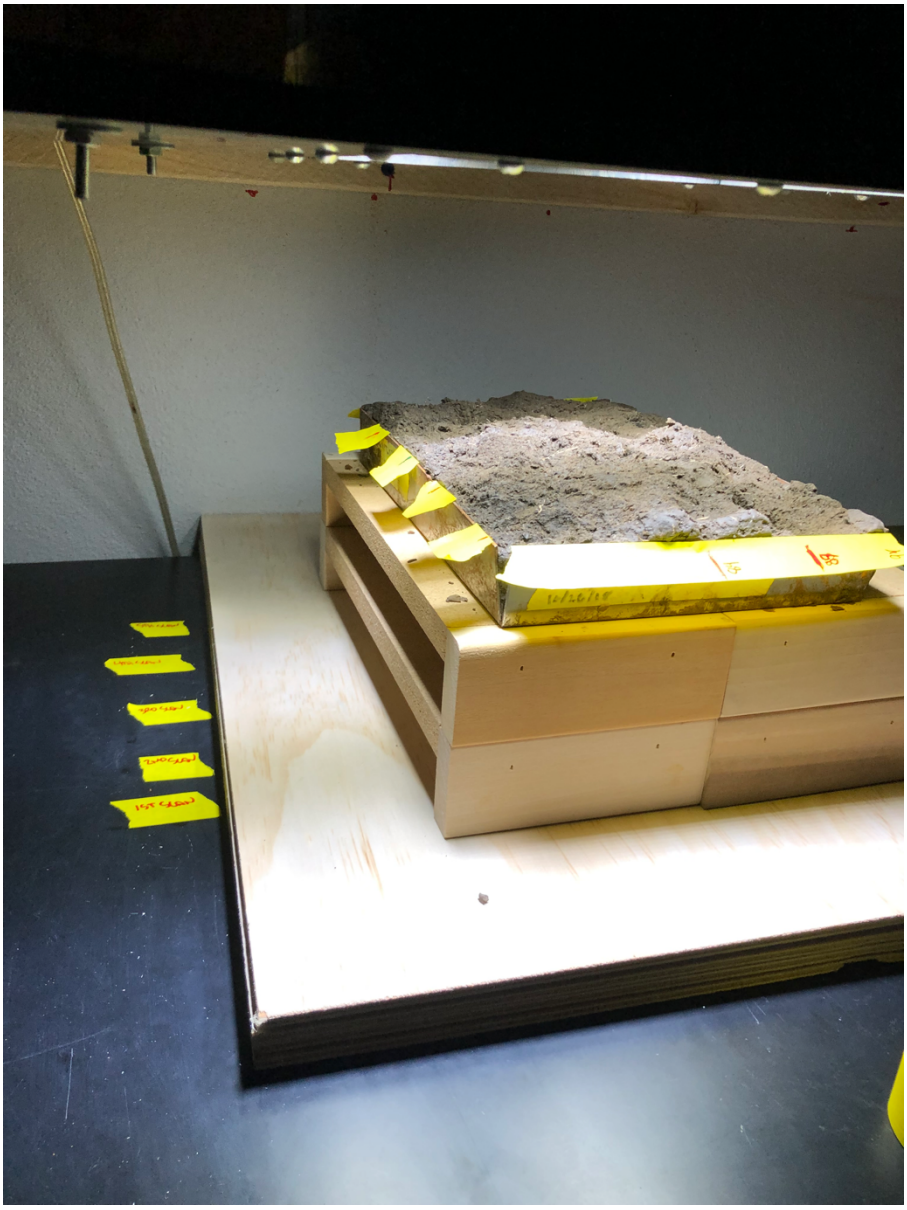

Figure 4.0 - The scanner will take a 2D photograph saved as a .jpg file before taking a 3D scan saved as a .scn file. These files will save together and overlap as one.

Analysis

Surface scanning gaps (SSGs) will be generated from the MLT scanning in order to generate relationships between the parameters listed below:

Files will be converted from .scn → .obj and processing will be performed in ImageJ.

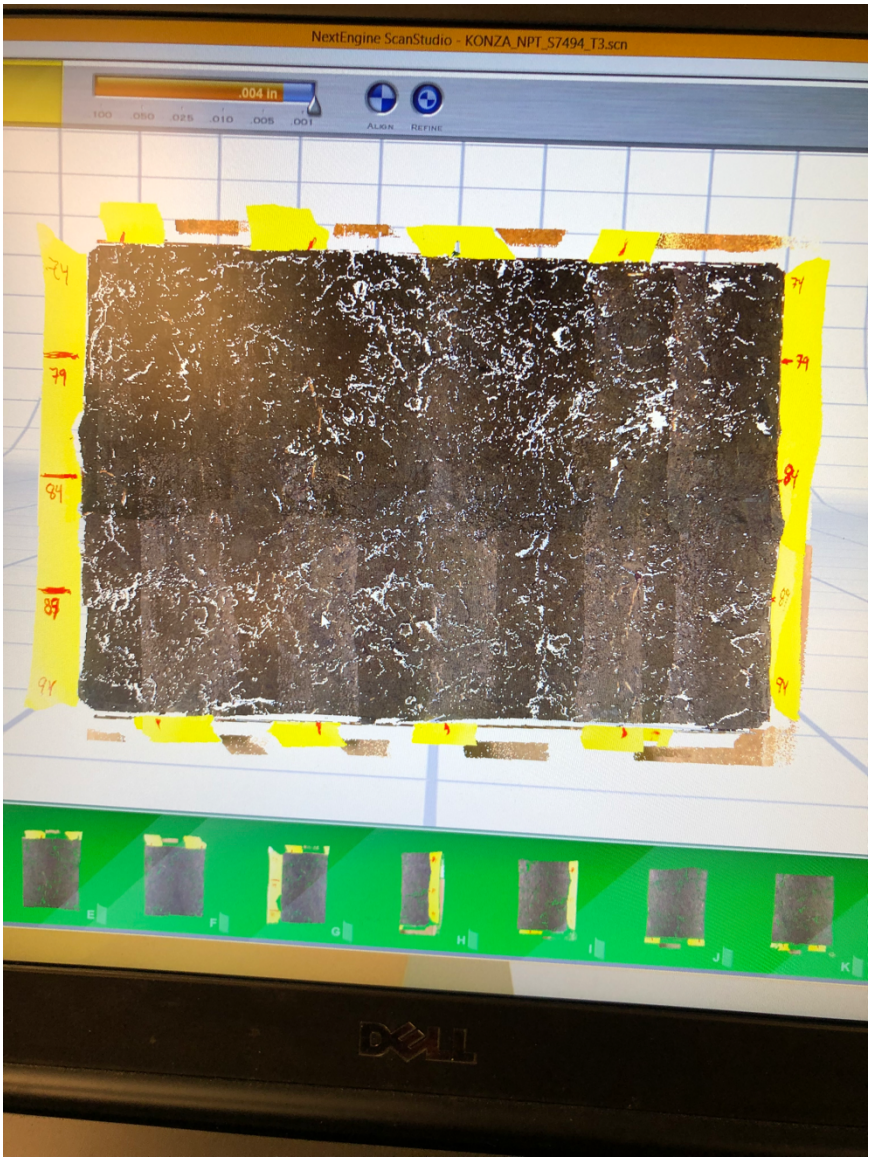

Figure 5.0 - After scanning and aligning the sub-scans, the resulting image will look something like this. The blank spaces are surface scan gaps (SSGs) and will be interpreted as macropores.

Trimming

1. Save aligned file as one ending in "_(trimmed)".
2. Save this file as one specific to the horizon being analyzed (remember that a tray may have multiple horizons, thus multiple files saved).

3. Once in the correct horizon file, use the "rectangular region selector" tool.
4. This tool will allow you to highlight the rectangular region of the tray that you wish to trim.
5. Highlight each side of the perimeter of the tray, trimming the measuring tape, tray edge, and surrounding blank spaces not captured by the scanner.

Saving as .xyz and Converting to .tiff in R

1. Before saving as a .xyz file, it is important to correct the orientation as close to 90-degree angles as possible.
2. To accomplish this, go to "CAD" → "Tools" → "Orient" → "Faces" in ScanStudio.
3. The objective is to make the bounding box as small as possible on all sides. Go through each side one-by-one.
4. The .scn file can now be saved as a .xyz file and processed in R. Make sure the resolution is set between 0.12-0.2 mm^2 (depending on the quality of the scan).
5. This file can be run through R in the program "20190619_ProximalSensingProject_RScript".
6. When running a new file, go to the bottom of the script and change the file name to the tray you wish to convert.
7. Two loading bars will result, and the conversion will be done when both bars reach 100%.
8. The resulting output file will go into the "Output" folder.

Analyzing .tiff in ImageJ

1. The perimeter of the .tiff file will still have to be cropped in ImageJ.
2. To crop, select the area of the image you want to include and press "shift-x" to remove the perimeter.
3. To set scale, go to "analyze", then "set scale".
4. Use the "straight line selection tool" to get a linear pixel count.
5. Multiply this pixel count by the resolution ($0.2mm^2$) to calculate a known distance (the scale should be set to 5 pixels/mm).
6. To check that this worked, use the line selection tool again from top-to-bottom of the sample and make sure the distance is reasonable (e.g. 154 mm).
7. Make sure that "global" is checked to apply to future images.
8. Click "set measurements" and check each box from "Area" → "Stack Position".
9. Two tables will be generated for each image -- the first is under "Measure" and the second is under "Analyze Particles".
10. The "Measure" table will automatically generate when selected but the "Analyze Particles" table will need special settings before being generated.

11. Settings -- size, pixel units, circularity, show:, display results, clear results, summarize, add to manager, exclude on edges, include holes, record starts, in situ show …
12. Information on pores larger than a sand grain will be recorded.

Reading Output Variable for Macropores in R

1. The output table will then be run in R for analysis.
2. From this, output variables will be quantified and related to each other in order to generate relationships on (X, Y, and Z) …

Analyzing Final Results

1. The output variables will also be related to collected NRCS data to generate further relationships on (X, Y, and Z) …

7.4 Appendix D: COLE Rod Procedure

Introduction

The Coefficient of Linear Extensibility (COLE) Rod method (Schafer & Singer, 1976) will be used in conjunction with the standard COLE method for estimating linear extensibility in shrink-swell soils (citation) performed by the NRCS. Using the COLE rod method will provide a better understanding of the degree of shrink-swell in 1-dimensional space, as opposed to the standard COLE method, which estimates total volumetric change in 3-dimensional space.

Materials

- 25-cm^3 syringes with 1-cm opening
- Plastic weigh boats
- Caliper
- Spatula
- 2-mm sieve
- 100g of < 2-mm sieved soil per horizon collected
- Rubber stopper and mortar
- 8-oz. paper cups
- Balance
- Metal weigh tins

- Autoclave

Procedure

1. Fill 8-oz. cups halfway with 100g of soil.
2. Add water and mix until paste is slightly less than saturated.
3. Let paste equilibrate for 24 hours and re-adjust moisture (paste should slightly glisten, but not flow when tilted (Black, 1965) -- the surface of the paste should be smooth after tapping cup on the table).
4. Remove plunger and insert paste into syringe using spatula.
5. Place the plunger back onto the syringe once filled with paste and extrude 3x rods that are 6 - 10cm in length.
6. Wet the spatula and trim rod ends perpendicular to the drying surface.
7. Measure and record the length and weight of the rods.
8. Re-measure the lengths and weights of the rods periodically at 2, 6, 24, and 48 hours.
9. Place air-dried rod in oven for 24-48 hours at 105C and take final weight measurement.
10. Calculate COLE rod using the following equation:

$$COLE_{rod} = (l_m - l_d) / l_d \qquad [1]$$

Where lm = length when moist (cm) and ld = length when dry (cm).

11. Calculate the air-dried gravimetric water contents (θ_2, θ_4, etc.) as using the following equation:

$$\theta_a = [(M_i - M_t) / M_t] - 1 \qquad \text{Eq. (2)}$$

Where M_i is the initial moisture content and M_t is the moisture content at a given time.

12. Calculate the oven-dried gravimetric water contents using the following equation:

$\theta_o = (M_i - M_{24}) / M_{24}$ Eq. (3)

Where M_i is the initial moisture content and M_{24} is the moisture content after drying for 24 hours.

13. Calculate the air-dried/ oven-dried ratio (ADOD) using the following equation:

$ADOD = \theta_a / \theta_o$ Eq. (4)

Using ADOD to have oven-dried values for each time-point.

14. Finally, using the known bulk density (ρ_b), calculate the specific volume corresponding to the appropriate gravimetric water contents for 2, 4, 8, and 24 hours:

$v_{s2} = [(COLE_2 + 1)^3] / \rho_b$ Eq. (5)